AGU PUBLICATIONS

JGR

Journal of Geophysical Research: Space Physics

RESEARCH ARTICLE
10.1002/2018JA025214

**Key Points:**
- A new set of Cassini plasma, energetic particle, and magnetic field data from Saturn's magnetosheath is introduced
- Statistical behavior of various magnetosheath properties is examined and compared with predicted upstream solar wind properties
- Science applications to electron heating at the bow shock and to magnetosheath structure are presented

**Supporting Information:**
- Supporting Information S1
- Data Set S1

**Correspondence to:**
M. F. Thomsen,
mthomsen@psi.edu

**Citation:**
Thomsen, M. F., Coates, A. J., Jackman, C. M., Sergis, N., Jia, X., & Hansen, K. C. (2018). Survey of magnetosheath plasma properties at Saturn and inference of upstream flow conditions. *Journal of Geophysical Research: Space Physics*, *123*, 2034–2053. https://doi.org/10.1002/2018JA025214

Received 9 JAN 2018
Accepted 24 FEB 2018
Accepted article online 1 MAR 2018
Published online 30 MAR 2018



# Survey of Magnetosheath Plasma Properties at Saturn and Inference of Upstream Flow Conditions

**M. F. Thomsen[1,2], A. J. Coates[3], C. M. Jackman[4], N. Sergis[5,6], X. Jia[7], and K. C. Hansen[7]**

[1]Planetary Science Institute, Tucson, AZ, USA, [2]Los Alamos National Laboratory, Los Alamos, NM, USA, [3]Mullard Space Science Laboratory, University College London, Dorking, UK, [4]Department of Physics and Astronomy, University of Southampton, Southampton, UK, [5]Office of Space Research and Technology, Academy of Athens, Athens, Greece, [6]Institute of Astronomy, Astrophysics, Space Applications and Remote Sensing, National Observatory of Athens, Athens, Greece, [7]Climate and Space Sciences and Engineering, University of Michigan, Ann Arbor, MI, USA

**Abstract** A new Cassini magnetosheath data set is introduced that is based on a comprehensive survey of intervals in which the observed magnetosheath flow was encompassed within the plasma analyzer field of view and for which the computed numerical moments are therefore expected to be accurate. The data extend from 2004 day 299 to 2012 day 151 and comprise 19,155 416 s measurements. In addition to the plasma ion moments (density, temperature, and flow velocity), merged values of the plasma electron density and temperature, the energetic particle pressure, and the magnetic field vector are included in the data set. Statistical properties of various magnetosheath parameters, including dependence on local time, are presented. The magnetosheath field and flow are found to be only weakly aligned, primarily because of a relatively large *z* component of the magnetic field, attributable to the field being pulled out of the equatorial orientation by flows at higher latitudes. A new procedure for using magnetosheath properties to estimate the upstream solar wind speed is proposed and used to determine that the amount of electron heating at Saturn's high Mach-number bow shock is ~4% of the dissipated flow energy. The data set is available as supporting information to this paper.

## 1. Introduction

Upstream from a planet immersed in a supersonic solar wind, a bow shock will form in order to slow and heat the incident wind, converting it to a subsonic flow that can be diverted around the obstacle (either the planetary atmosphere/ionosphere or the magnetosphere). The region of shocked solar wind that exists between the bow shock and the obstacle is the magnetosheath, and its plasma conditions are determined by the physical processes that take place within the shock, processes that are known to vary with upstream plasma properties such as Mach number and interplanetary magnetic field orientation. For a magnetized planet whose intrinsic magnetic field enables it to form a magnetosphere, the interaction between the solar wind and the magnetosphere is mediated by the magnetosheath, and the processes that occur at the magnetopause are determined by the properties of the magnetosheath plasma and of the magnetospheric plasma just inside the magnetopause.

Saturn's magnetosheath is of particular interest to comparative magnetospheric physics for two principal reasons: (1) the evolution of solar wind properties with heliocentric distance is such that at the outer planets the Mach number of the flow is typically higher than at the Earth (e.g., Jackman & Arridge, 2011; Masters et al., 2011; Slavin et al., 1985) and (2) the nature of Saturn's magnetosphere is strongly influenced by its rapid rotation, internal plasma sources (especially the moon Enceladus), and strong internal magnetic field. These latter features combine to produce very fast corotational flow inside the magnetosphere (e.g., Thomsen et al., 2010) and strong centrifugal distension of the equatorial region, leading to polar flattening of the magnetopause (e.g., Slavin et al., 1985; Stahara et al., 1989; Sulaiman et al., 2014, 2017) and other nonaxisymmetries (e.g., Kivelson & Jia, 2014; Pilkington et al., 2015).

In light of these differences in both the upstream and internal plasma properties, it is quite likely that various physical processes take on a different level of importance for Saturn compared to the Earth. For example, the higher Mach number of the solar wind flow causes a higher magnetosheath β (ratio of particle pressure to

magnetic pressure), which in turn may suppress magnetopause reconnection (Masters, Eastwood, et al., 2012). Likewise, strong shears between flows in the magnetosheath and in the magnetosphere can also suppress reconnection (e.g., Desroche et al., 2013; Fuselier et al., 2014). As another example, the action of the Kelvin-Helmholtz (K-H) instability at the magnetopause depends on magnetosheath properties, especially the magnetic field orientation and the flow shear across the magnetopause (e.g., Desroche et al., 2013). There is some indication that K-H activity at Saturn is more prominent in the afternoon and dusk sector than was first anticipated (e.g., Delamere et al., 2013; Masters, Achilleos, et al., 2012), perhaps because magnetospheric flows transport K-H vortices formed prenoon on around to the afternoon magnetopause region (Delamere et al., 2013; Ma et al., 2015).

In addition to the influence that magnetosheath properties have on the coupling between the solar wind and the magnetosphere, the properties themselves are reflective of the collisionless physics of the bow shock. With generally higher upstream Mach numbers than at Earth, Saturn's bow shock provides a laboratory for the study of the physics of very high Mach number shocks (e.g., Masters et al., 2011; Masters et al., 2016; Richardson, 1987; Sulaiman et al., 2016, 2015). For example, one plasma property that has been found to vary with Mach number is the downstream ratio of the ion and electron temperatures. This quantity is of particular interest to magnetospheric studies inasmuch as it provides a potential marker for solar wind entry into the magnetosphere (e.g., Lavraud et al., 2009).

Prior to the arrival of Cassini in 2004, Saturn's magnetosheath had been visited by 3 flyby missions: Pioneer 11 (1979), Voyager 1 (1980), and Voyager 2 (1981). Cassini's 13 year orbital mission has vastly extended the magnetosheath observations, both with regard to spatial coverage and with regard to the range of upstream conditions. These observations have enabled statistical studies of the location of Saturn's bow shock and magnetopause (e.g., Arridge et al., 2006; Kanani et al., 2010; Masters et al., 2008; Pilkington et al., 2014, 2015; Went et al., 2011), as well as the magnetic field structure (e.g., Sulaiman et al., 2014) and turbulence (e.g., Hadid et al., 2015) within the magnetosheath. Evidence has been found for the existence of a plasma depletion layer (Masters et al., 2014) and K-H waves at the magnetopause (e.g., Delamere, Wilson, & Masters, 2011; Delamere et al., 2013; Masters et al., 2009, 2010). A study of 70 magnetopause crossings found that the magnetosheath $\beta$ is typically high, restricting magnetopause reconnection to regions where the magnetic fields on either side are more nearly antiparallel (Masters, Eastwood, et al., 2012).

With regard to the physics of the bow shock itself, Masters et al. (2011) studied the electron heating at 94 Cassini bow shock crossings and found that the amount of electron heating across the shock represents between ~3% and ~7% of the incident solar wind ram energy, with a clear decline in the fraction with increasing Alfvén Mach number. This range is comparable to values found at Earth of ~7% (Schwartz et al., 1988; Thomsen et al., 1987).

The most extensive survey of Saturn's magnetosheath properties was done by Sergis et al. (2013), who examined Cassini plasma, magnetic field, and energetic particle measurements in the magnetosheath for 7 years of the Cassini mission. Restricting the study to intervals where the spacecraft remained within the magnetosheath for 24 hr or more, they found 916 hr of data. Of these, only 340 hr had reliable plasma moments because Cassini was often oriented in such a way that the trans-sonic magnetosheath flow was not directed into the Cassini Plasma Analyzer/Ion Mass Spectrometer (CAPS/IMS) field of view (FOV). That FOV is nearly $2\pi$ sr (Young et al., 2004), but the constraints imposed by the requirements of the imaging instruments and thermal balance nonetheless frequently prevented IMS from seeing the flow (cf. Thomsen et al., 2010). Further, the fact that Cassini was commonly rolling about different axes as it orbited Saturn makes determination of the ion moments problematic, and the moments determined from numerical integration of the observed distributions according to the method described in Thomsen et al. (2010) are flagged as being incorrect under such rolling conditions.

In spite of these limitations on the availability of thermal plasma measurements, Sergis et al. (2013) established important facts about Saturn's magnetosheath: typical flow directions; ranges of density, temperature, and flow speed; typical values of plasma $\beta$; and the relative distributions of plasma, energetic particle, and magnetic pressures. The study particularly focused on the frequent presence of high-energy water-group ions (designated W+) within the magnetosheath plasma, which demonstrates that energetic particles are able to leak from the magnetosphere and escape both downstream within the magnetosheath and upstream into the unshocked solar wind.

The difficulty of obtaining valid plasma ion moments has limited the scope of several of the studies mentioned above. For those studies, the determination of which ion moments are likely to be trustworthy has been done on a case-by-case basis, which limits the number of events that can practically be included. In order to improve the event statistics without examining the viewing for every spectrum, Burkholder et al. (2017) used the viewing flag provided with the IMS moments data at the Planetary Data System (PDS) repository with a simple binary criterion: In the postnoon region of the magnetosheath, the magnetosheath flow ought to be largely in the $+\phi$ direction (in a Kronographic r, $\theta$, $\phi$ coordinate system), which is parallel to the strict corotational direction inside the magnetosphere, so if the FOV includes the corotational direction (the definition of the viewing flag), the flows were accepted as valid measurements. On the other hand, in the prenoon sector, flows were accepted as valid only if the flag indicates that corotation is not in the FOV. Burkholder et al. (2017) presented persuasive evidence that this procedure satisfactorily identified valid magnetosheath flow speeds. They used the resulting data set to demonstrate a prenoon/postnoon asymmetry in flow speed, which was interpreted as evidence for momentum coupling across the magnetopause. While this approach allowed a satisfactory estimate of the flow speed, the corresponding densities and individual flow components may not be at all well determined if the bulk flow does not lie within the CAPS FOV. It is therefore highly desirable to establish more definitively which CAPS magnetosheath ion moments are expected to be valid.

The purpose of the present report is to introduce a new Cassini magnetosheath data set that is based on a comprehensive survey of magnetosheath intervals to identify those in which the observed magnetosheath flow was encompassed within the CAPS FOV and for which the numerical moments are therefore expected to be accurate. This expands and extends the work of Sergis et al. (2013) by including many intervals of duration less than 24 hr and by including additional CAPS observations from 2011 until the instrument was turned off in 2012. The observations thus span the interval from the descending phase of solar cycle 23 through the ascending phase of cycle 24. In addition, we have merged this data set with corresponding time averages of the electron moments (density and temperature) from the CAPS Electron Spectrometer (ELS) ( Young et al., 2004), energetic particle pressures from the Magnetosphere Imaging Instrument (MIMI) (Krimigis et al., 2004), and magnetic field measurements from the Cassini Fluxgate Magnetometer (MAG) (Dougherty et al., 2004). We anticipate that this new data set, available as supporting information to this paper, will enable a number of in-depth studies of Saturn's magnetosheath, and we provide here several examples of its utility for addressing important scientific questions.

## 2. Data Analysis

The CAPS IMS is a top-hat electrostatic analyzer (for energy-per-charge determination) followed by a time-of-flight section (for particle speed determination). There are eight anodes, providing eight different look directions in the viewing plane. Azimuthal coverage is provided by a physical actuator, which sweeps the viewing plane back and forth, resulting in coverage of ~$2\pi$ sr of the sky. The energy range of the instrument is ~1 eV–50 keV. For further instrumental details, see Young et al. (2004) or Thomsen et al. (2010).

The ion moments from CAPS/IMS that are used in this study, as in the previous works cited above, is the set of numerical moments derived from the Singles (SNG) data product, as described by Thomsen et al. (2010), with one exception: The ions with m/q = 2 are assumed to be $H_2^+$ in that data set since the dominant sources of such particles within the magnetosphere are the water emitted from Enceladus and Titan's upper atmosphere. For the present work, ions with m/q = 2 in the magnetosheath are assumed to be shocked solar wind $He^{++}$. Since the calculated temperature (Thomsen et al., 2010) depends on both m/q and q itself (density and flow velocity depend only on m/q), the temperature in the original file has been multiplied by a factor of 2.

In preparation for submission of the Thomsen et al. (2010) moments to the PDS, the CAPS team undertook a cross calibration of the derived ion densities with the electron densities determined from the Cassini Radio and Plasma Wave Science (Gurnett et al., 2004) experiment. The latter are based on identification of wave emissions near the upper hybrid frequency and are judged to provide the most accurate estimate of the local electron density. This comparison resulted in a slight adjustment of the IMS detection efficiencies, which was incorporated in a re-run of the data included in the Thomsen et al. (2010) study, as well as all subsequent calculated SNG moments. Use of the new efficiencies made only fairly slight differences in the derived densities

of the different ion components (generally less than ~20% either way) compared to values used by Thomsen et al. (2010), and velocities and temperatures were unchanged. The full CAPS/IMS/SNG numerical moment data set with the final efficiencies is now publicly available at the PDS. Each value is based on 416 s of data (13 A-cycles), which allows data to be included from a full actuation cycle, thereby giving the fullest possible angular coverage.

In addition to the CAPS IMS numerical moments, this data set includes CAPS ELS electron moments, specifically the electron density and temperature calculated from numerical integration of the observed counts (Lewis et al., 2008) and now available at the PDS. Like IMS, ELS is a top-hat electrostatic analyzer with eight separate anodes viewing parallel to the IMS anodes and covering an energy range of ~0.6 eV–28 keV (Linder et al., 1998; Young et al., 2004). As with IMS, the physical actuation of the CAPS instrument allows ELS to scan ~$2\pi$ sr of the sky. The ELS moments available at PDS use measurements from anode 5 only, assuming an isotropic distribution (Lewis et al., 2008). To include these moments in the data set, we average the ELS values from the PDS (i.e., only anode 5) over the 416 s covered by each IMS/SNG moment calculation.

The Cassini magnetic field investigation (MAG) (Dougherty et al., 2004) is a combination of two magnetometers: a vector helium magnetometer and a fluxgate magnetometer. Magnetic field measurements are made with a high temporal cadence ($\geq$1 measurement per second), but we have averaged the data to match the 416 s CAPS measurement interval. The tabulated data consist of three components in the KRTP coordinate system, plus the field magnitude. In addition to the 416 s mean values that are used in this paper, the data file also includes the median values of the components and magnitude for the same 416 s intervals. Intervals that fell within MAG data gaps or during SCAS intervals (Science Calibration Subsystem, see Dougherty et al., 2004) are flagged with fill values of $-$9999.99.

The MIMI (Krimigis et al., 2004) measures energetic ions (3 keV/e to few MeV/e) and electrons (20 keV to 1 MeV). The energetic ion pressure determined from the MIMI CHEMS (Charge Energy Mass Spectrometer) and LEMMS (Low Energy Magnetospheric Measurement System) measurements (cf. Sergis et al., 2017) is interpolated to the CAPS time cadence from a tabulation of 10 min values, derived as described by Sergis et al. (2009). Intervals where MIMI data are not available are flagged with pressure values of $-$1.0000.

As noted above, when the CAPS instrument is actuating, its FOV is ~$2\pi$ sr. For hot, slow flows, this is quite adequate for CAPS to characterize the full ion distribution (except for the flow velocity). However, throughout much of the Saturnian magnetosphere and magnetosheath, flow speeds are comparable to or greater than the thermal speed of the ions, so to properly characterize the plasma (density, flow, and temperature), the instrument FOV needs to encompass the flow. Further, when the spacecraft is rolling or if CAPS is not actuating, the computational algorithm for the SNG numerical moments yields incorrect values. Thus, to obtain trustworthy ion moments for the present study, it was necessary to identify time intervals when the magnetosheath flow was in the CAPS FOV and when the instrument was actuating and the spacecraft was not rolling. Note that while the flow direction must lie within the CAPS FOV, it is acceptable if it lies very near the edge of the FOV since the computational algorithm mirrors the distribution about the flow direction (cf. Thomsen et al., 2010).

Accordingly, we conducted a comprehensive by-eye survey of the entire CAPS/IMS data set (from Saturn Orbit Insertion on 30 June 2004 to 1 June 2012) to identify all such intervals with duration of at least 1 hr. Using 6 hr production energy-time spectrograms of the SNG and ELS count rates, available on the Los Alamos National Laboratory website (http://www.caps.lanl.gov/cgi-bin/tdc_search.cgi), we identified intervals when Cassini was clearly within the magnetosheath, based on the ion and electron spectral shape as illustrated below. Consulting FOV plots available on the same website, we then excluded intervals when the spacecraft was rolling, CAPS was not actuating, or the magnetosheath flow was not in the CAPS FOV.

Figure 1 shows two 6 hr intervals in which good-quality magnetosheath parameters could be obtained. Figures 1a–1e show an interval on 24 September 2009 (day 267) when Cassini passed from the magnetosheath into the solar wind and then back into the magnetosheath. The magnetosheath population is characterized by ion energies between ~100 eV and ~2 keV and electrons up to about 100 eV. The solar wind is best identified in the electrons, which have energies generally below 10 eV (and in the ELS energy ranges are probably dominated by spacecraft-originating photoelectrons). If the solar wind ion population is within the

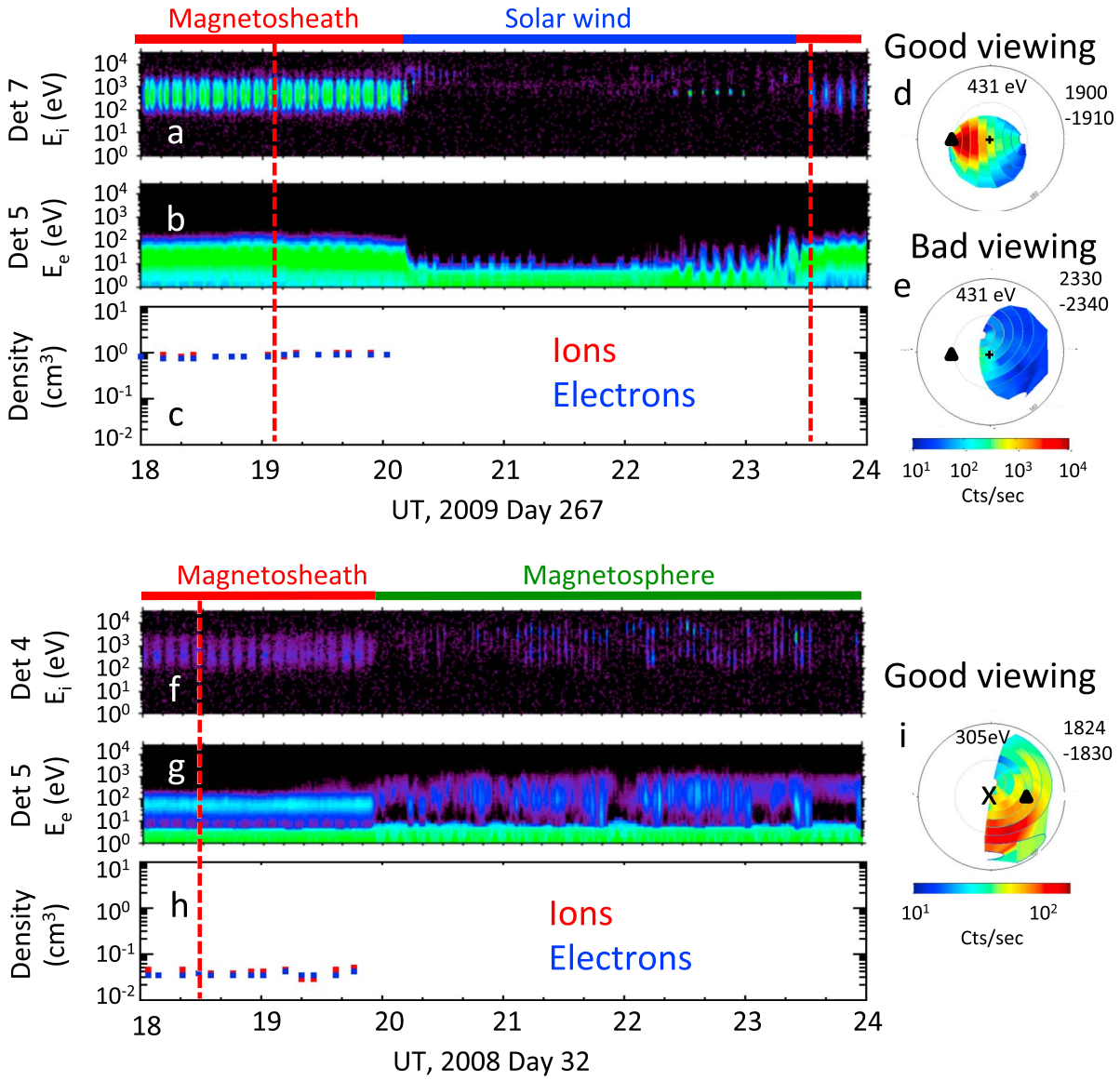


**Figure 1.** Examples of magnetosheath intervals with suitable CAPS viewing: (a–e) From 24 September 2009; (f–i) from 1 February 2008. (a) Color-coded counts per accumulation interval (proportional to energy flux) of ions in the SNG (E/q identification only) data product of CAPS/IMS, as a function of E/q and time. Data are from detector 7, which contained the peak count rate of the distribution. (b) Corresponding electron count rate (again proportional to energy flux) versus E and t from ELS detector 5. (c) Ion (red) and electron (blue) densities reported in the new magnetosheath data set. No values are reported from the interval in the solar wind (blue bar above panel a), nor from the magnetosheath interval between 2300 and 2400 UT, when the heart of the ion distribution was not in the CAPS field of view (FOV). (d) All-sky viewing plot of counts observed at 431 eV between 1900 and 1910 UT (time marked by vertical red dashed line on panels (a–c)). The plus sign at the center of the circle indicates the look direction toward Saturn, and the black triangle to the left of that indicates the look direction where corotation would be expected. The thin circle half-way between the plus sign and the outer circle corresponds to look directions in the plane perpendicular to the radial direction, with the northward looking direction at the top of the circle. The peak counts of the observed angular distribution lie within the FOV of CAPS, so the derived moments are deemed valid for this interval. (e) Same as panel d, for 2330–2340 UT, during the second encounter with the magnetosheath (marked by second red dashed line in panels (a–c)). In this case the peak of the ion count distribution does not seem to have been captured by the CAPS FOV, so the ion moments are not deemed valid, and this interval is excluded from the data set. (f–i) Same as (a–e) except for an energy of 305 eV during a 6 hr interval on 1 February 2008, during which Cassini moved from the magnetosheath across the magnetopause into the magnetosphere. The all-sky viewing for 1824–1830 UT illustrated in panel (i) is reversed from that shown in panels (d and e): The *x* at the center of the plot now corresponds to the look direction away from Saturn. The black triangle still shows the look direction for corotation, and northward looking is still at the top of the light circle half-way from the center to the outer circle.

CAPS FOV, it shows up as the very narrow population at ~1 keV seen between ~2230 and 2300 UT. The disappearance of ~keV ions upon crossing the bow shock into the solar wind at ~2010 UT (Figure 1a) indicates that while the magnetosheath flow was into the CAPS FOV, the solar wind itself was not. Near the end of the solar wind interval, the solar wind distribution just barely makes an appearance, and it is

clear that the highly supersonic distribution there is qualitatively quite different from the hot, trans-sonic magnetosheath plasma seen earlier. Thus, it is quite easy to distinguish magnetosheath from solar wind on the basis of both the ion and the electron energy distributions.

At ~2325 UT, the change in the spectral properties of both ions and electrons indicates a return to the magnetosheath. However, while the electron spectrum looks quite similar to what was seen before the first bow shock crossing at ~2010 UT, the ion counts are much reduced compared to the earlier magnetosheath interval. This suggests that the distribution was no longer flowing into the CAPS FOV, so IMS missed the bulk of the plasma. The two field-of-view plots to the right of the spectrograms (Figures 1d and 1e, corresponding to times marked by red vertical lines in Figures 1a–1c) confirm this conclusion: Figure 1d shows the all-sky distribution of ion counts at 430 eV for a 10 m period starting at 1900 UT, in the first magnetosheath interval, whereas Figure 1e shows the same thing for the 10 m period starting at 2330 UT, in the second magnetosheath interval. Figure 1d shows that in the first interval the peak of the ion flux was well captured within the CAPS FOV, while Figure 1e shows that in the second interval, the peak very probably lay beyond the edge of the FOV. Thus, in this 6 hr interval, only the earlier time in the magnetosheath (1800–2000 UT) was included in the database. The included ion and electron densities within the magnetosheath from the database are shown in Figure 1c.

Figures 1f–1i show similar data from 1 February 2008 (day 32). In this case, the first ~2 hr of the interval occurred in the magnetosheath, as evidenced by the presence of ions between ~100 and 1,000 eV and electrons in the neighborhood of 30 eV. The spectral shapes of both ions and electrons are similar to those in Figures 1a and 1b, but the intensities are considerably lower (same color bar for both intervals), as shown by the much lower densities derived for both species. At ~1950 UT, Cassini crossed the magnetopause into the magnetosphere, characterized by hotter and quite variable electron distributions and very weak ion fluxes with two evident peaks in energy corresponding to magnetospheric water group ions and magnetospheric protons. As with the solar wind, the spectral properties of the magnetospheric populations are qualitatively quite different from those in the magnetosheath. The field-of-view plot in Figure 1i shows that the magnetosheath ion distribution was within the CAPS FOV during this interval, so the moments are likely to be valid (as for Figure 1c, the derived ion and electron densities were nearly equal, indicating that the low derived densities in the second event are real and not just indicative of missing the main magnetosheath ion population). Figure 1 thus illustrates that it is generally quite easy to identify magnetosheath plasma on the basis of its spectral characteristics. It also illustrates the means by which we can determine if the flow lies within the CAPS FOV.

The survey of the entire CAPS data set from Saturn Orbital Insertion to the date when CAPS was turned off yielded 657 separate magnetosheath intervals, comprising a total of 19,155 valid measurements (2,213 hr). For each CAPS/IMS measurement that was judged to meet the selection criteria, the quantities tabulated in the file described here are as follows:

1. Date (day.frac of 2004)
2. Date (day.frac of actual year)
3. Year
4. Day of year (DOY)
5. Time (hour, minute, second)
6. Spacecraft location (radial distance, SSQ latitude, SSQ local time)
7. Thermal H+ density, temperature, flow velocity (KRTP components)
8. Thermal He++ density, temperature, flow velocity (KRTP components)
9. Thermal electron density, temperature, number of data points in average
10. Magnetic field magnitude and components (KRTP coordinates), both mean and median values for the CAPS/IMS moments interval; also given are the standard deviations of those mean values. In this paper we use only the mean values.
11. Energetic ion pressure

The SSQ (inertial Saturn-centered equatorial) coordinate system is defined as *z* parallel to Saturn's rotational/dipole axis ($\widehat{\Omega}_S$), *x* toward the Sun in the plane containing the *z* axis and the Saturn-Sun direction, and *y* completing the right-handed system. The KRTP (Kronocentric r, $\theta$, $\phi$) coordinate system has positive $\widehat{r}$ radially outward from Saturn, $\widehat{\varphi}$ in the direction of $\widehat{\Omega}_S \times \widehat{r}$, and $\widehat{\theta}$ in the direction $\widehat{\varphi} \times \widehat{r}$.

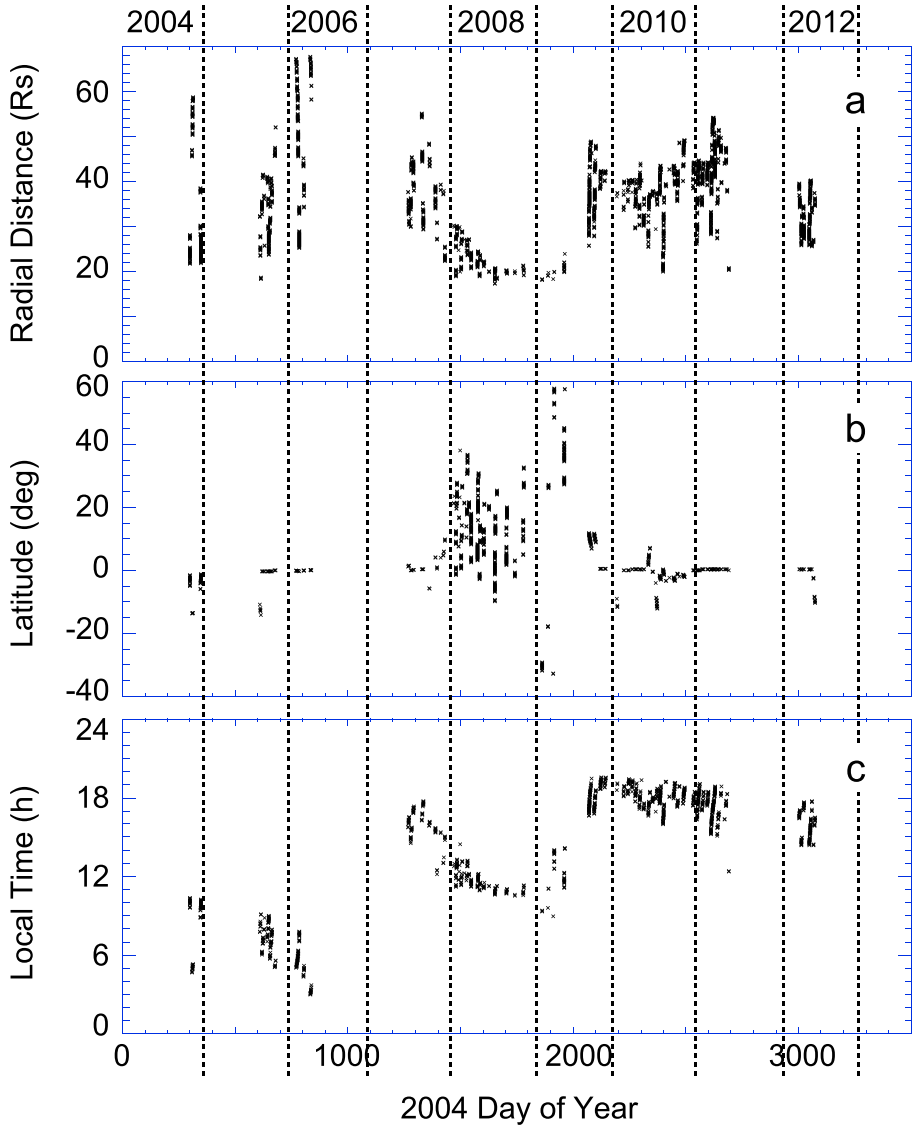


**Figure 2.** Summary of coverage for valid magnetosheath measurements included in the new data set. (a) Radial distance, (b) Kronographic latitude, and (c) local time. Values are plotted as a function of day of year 2004 (i.e., days since the beginning of 2004), and the corresponding years are shown above panel (a) and demarcated by vertical dashed lines.

## 3. Statistical Results

### 3.1. Coverage

Figure 2 summarizes the spatial locations (radial distance, SSQ latitude, and local time) at which valid measurements have been identified. The parameters are plotted as a function of DOY 2004, and the corresponding years are noted above the upper panel. The coverage is largely determined by the evolution of the orbit over the course of the Cassini mission. For example, detection of magnetosheath signatures at very large radial distances primarily occurs in the 2006 time frame, when Cassini apoapsis was at very early local times; that is, the magnetosheath was seen far down on the dawn flank of the magnetosphere. Similarly, high-latitude magnetosheath encounters occurred during 2008 and 2009, when the orbital plane was strongly inclined to Saturn's equatorial plane, and apogee was near noon local time. The radial distance and latitude versus local time distribution of the magnetosheath intervals is shown explicitly in Figure 3.

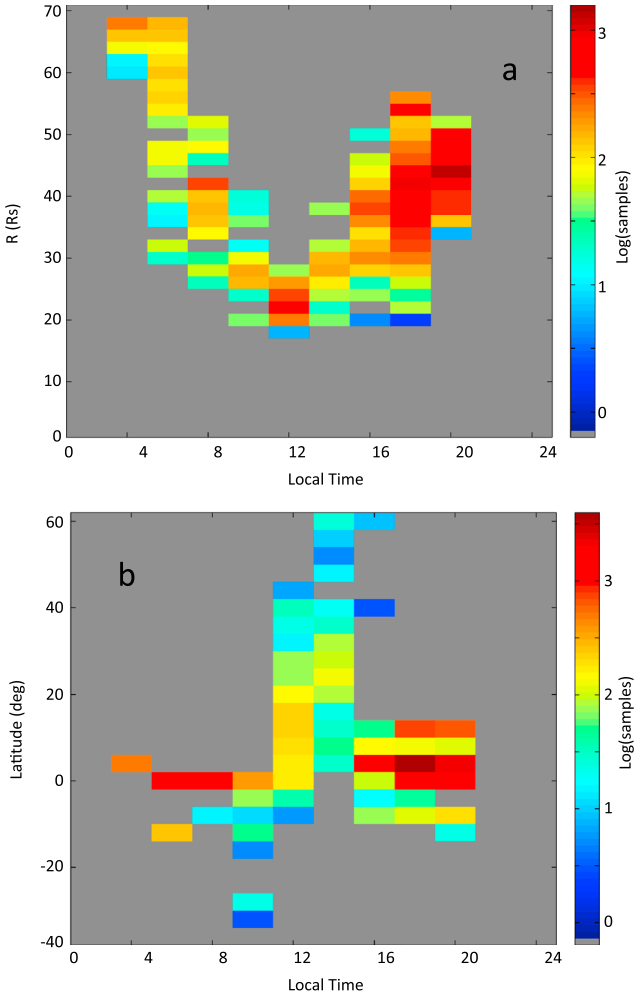


**Figure 3.** Number of valid magnetosheath measurements obtained in bins of local time and (a) radial distance or (b) latitude.

### 3.2. Occurrence Distributions

Figure 4 shows histograms of various magnetosheath properties from the entire data set. Figure 4a shows the occurrence distribution of measured values of the alpha particle-to-proton ratio (thick black line), compared to a similar distribution from daily averages of the solar wind alpha-to-proton ratio available from the OMNI database of near-Earth measurements (2004 DOY 180 to 2012 DOY 180, thin black line). Note that the distributions are not normalized to the total number of measurements in either case. While densities, temperatures, and flow velocities all change between 1 and 10 AU, the composition of the solar wind should remain constant. Compared to the OMNI distribution (largely drawn from ACE measurements), our Saturn magnetosheath ratio has a relatively lower occurrence of low values and a relatively higher occurrence of high values, although the bulk of the distribution is similar to the near-Earth values. The near-Earth median (0.0270) and mean (0.0298) are slightly smaller than we find from our magnetosheath data (0.0349 and 0.0375, respectively, as marked on Figure 4a).

Figure 4b shows the unnormalized occurrence distribution of measured values of the proton-to-electron density ratio for the full data set (heavy line) and for two subsets of the data (light lines). The full data set shows a peak occurrence near 1.5, with a secondary peak near 3. In examining the time history of this ratio, it appears that there was a general step down in the ratio sometime between 2006 DOY 108 (2004 DOY = 840) and 2007 DOY 172 (2004 DOY = 1268). We believe that this step may have been due to an adjustment of the ELS microchannel plate voltage performed on 6 June 2006, which increased the efficiency for electron detection. The light lines in Figure 4b show the distributions prior to and after this adjustment. While it seems plausible that there was a discrete change in the electron detection efficiency between these two intervals, it is also possible that the absolute ion detection efficiency of IMS declined during the period, so we have made no adjustments to any of the reported densities in our data set.

Setting aside the question of the discrete step down in the proton-to-electron density ratio, Figure 4b indicates that, in general, the derived proton densities exceed the derived electron densities. Since the density ratio should be near 1.0 (actually, slightly less since the alpha particles also contribute to the charge balance), we conclude that there is some remaining uncertainty in the absolute efficiency of either or both of the instruments. There is also the possibility that significant pitch angle anisotropies in the electron population may affect the determination of the electron densities since they were derived solely from measurements from a single anode, which may or may not have had sufficient pitch angle coverage to accurately represent an omnidirectional integration of the distribution in any given interval. However, we would expect this effect to cause a spread in the derived ratio, rather than a general offset. Hence, uncertainties in the absolute detection efficiencies seem the likeliest explanation. For users of this magnetosheath data set, we therefore recommend adopting an average of the reported proton and electron densities, with a corresponding uncertainty equal to half their difference. For composite properties in the remainder of this paper (such as beta or Mach number), we adopt this average density.

Figure 4c shows the occurrence distribution of the proton-to-electron temperature ratio within Saturn's magnetosheath. With an average near 9 and a 5–95% range of ~5–15, the temperature ratio is very similar to typical values in the Earth's magnetosheath (e.g., Phan et al., 1994).

Figure 4d shows the occurrence distribution of the plasma beta, defined as

$$\beta = 8\pi nk\left(T_p + T_e\right)/B^2 \quad (1)$$

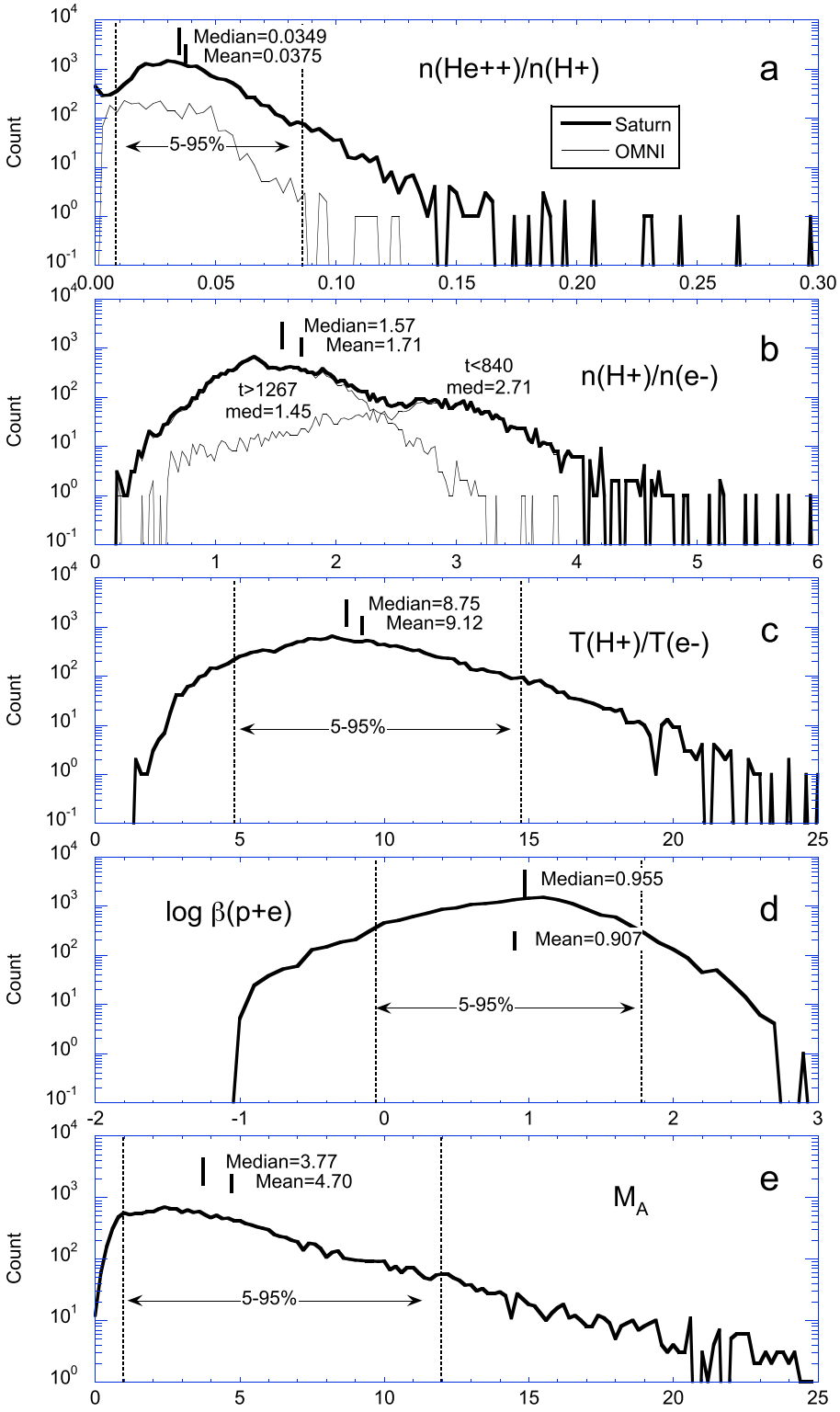


**Figure 4.** Occurrence histograms of various magnetosheath properties: (a) ratio of alpha-particle density to proton density, (b) ratio of derived proton density to derived electron density, (c) ratio of proton temperature to electron temperature, (d) logarithm of the plasma beta (protons + electrons), and (e) Alfvén Mach number of the magnetosheath flow. The light line in (a) shows the abundance ratio measured near Earth for the same time interval, as listed in the OMNI database. The light lines in (b) show the distributions for subsets of the total interval, from prior to 2004 DOY 840 (2006 108) and from after 2004 DOY 1267 (2007 172). Means and medians are shown for all parameters, and the 5–95 percentile range for all parameters except the ion-to-electron density ratio.

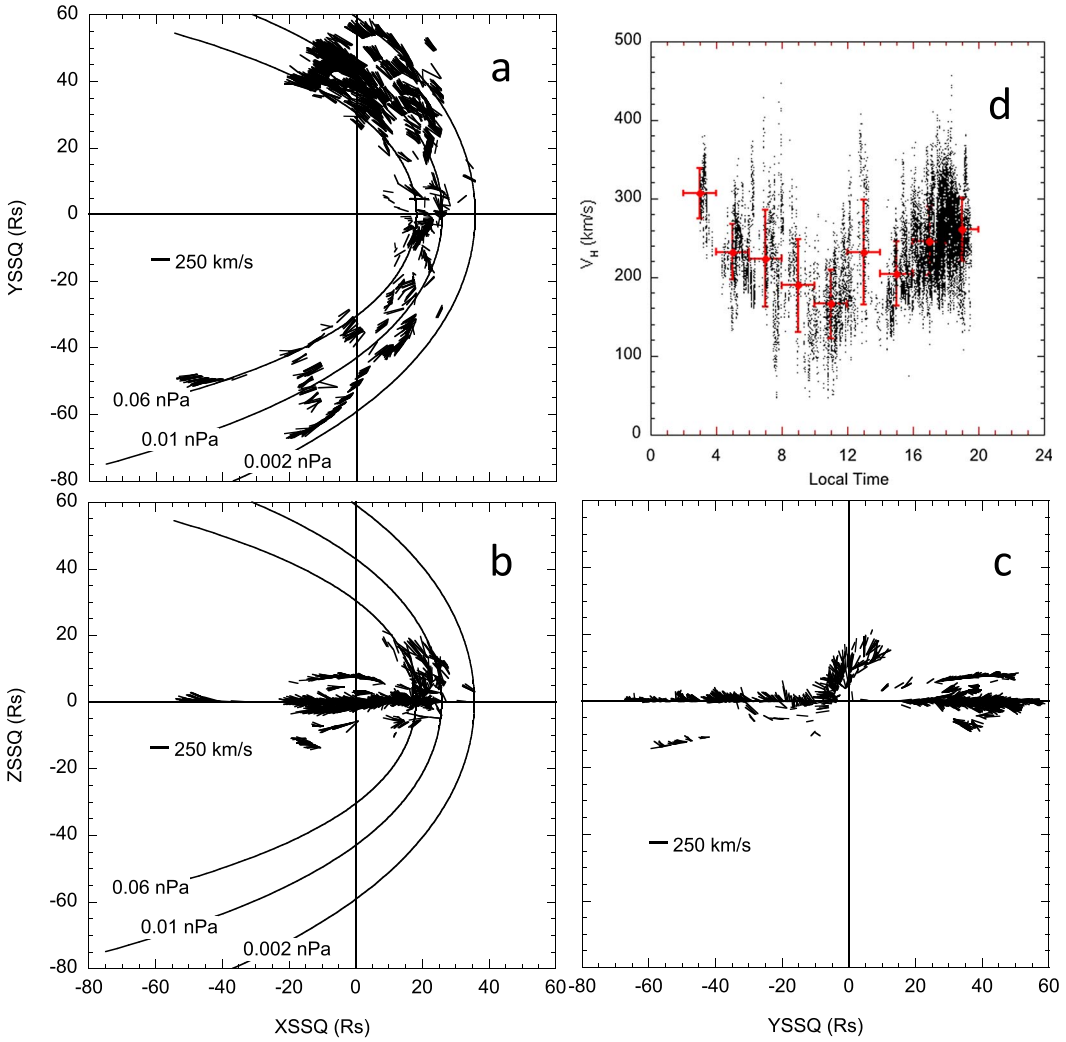


**Figure 5.** Plane projections of the measured magnetosheath flow directions in SSQ coordinates: (a) *x-y*, (b) *x-z*, and (c) *y-z*. Scale is 50 km/s = 1 Rs. Only every tenth measurement in the data set is shown. The solid curves in (a and b) are the Kanani et al. (2010) magnetopause locations for solar wind dynamic pressures of 0.002, 0.01, and 0.06 nPa. (d) Total measured flow speed as a function of local time. The red points show the flow speed averaged in 2 hr local time bins. The horizontal error bars simply show the 2 hr ranges, and the vertical error bars show the standard deviation of the averages.

where $n$ is the average density recommended above, $T_p$ and $T_e$ are the proton and electron temperatures, and $B$ is the average field magnitude. The $k$ is the Boltzmann constant. The distribution shown in Figure 4d is in general agreement with the beta values reported by Masters, Eastwood, et al. (2012) and Sergis et al. (2013): Very few samples (<6%) have beta values of less than 1, while a large fraction (>50%) have values greater than 10, and the distribution extends into the hundreds. Moreover, the plasma pressure plotted in Figure 4d does not include the energetic particle pressure, which often contributes half or more of the total magnetosheath pressure (Sergis et al., 2013; see Figure 10 and associated discussion below), so the total beta distribution would be shifted to greater values compared to Figure 4d.

Finally, Figure 4e shows the occurrence distribution of the local Alfvén Mach number

$$M_A = V/V_A = V\sqrt{4\pi n m_p/B^2} \tag{2}$$

where $V$ is the magnitude of the proton velocity measured by IMS, $V_A$ is the Alfvén speed, and $m_p$ is the proton mass. Ninety-five percent of the flows in the magnetosheath are found to be super-Alfvénic.

### 3.3. Flow Velocities

Figures 5a–5c show the *x-y*, *x-z*, and *y-z* plane projections of the measured flow velocities in the SSQ coordinate system. The vectors are scaled to 1 Rs = 50 km/s. For clarity of presentation, only every tenth measurement is shown. The solid curves are the Kanani et al. (2010) magnetopause locations for solar wind dynamic pressures of 0.002, 0.01, and 0.06 nPa. This range (0.002–0.06 nPa) fully encompasses the range of observed values compiled by Jackman and Arridge (2011). The vectors are reasonably well encompassed by these curves and clearly show the expected deflection around the magnetosphere, in both the equatorial plane and out of it at higher latitudes. Figure 5d shows the total measured flow speed of the protons plotted as a function of local time. The red circles indicate averages of the flow speed in 2 hr local time bins. The vertical red bars show the standard deviation of the averages. As expected, the flow speed is lowest near noon and increases along the flanks as the shocked flow reaccelerates toward the upstream flow speed.

### 3.4. Local Time Dependence

As seen in Figure 5d, magnetosheath properties clearly depend on the local time of the measurements. Figure 6 shows the local time dependence of several representative magnetosheath properties. For this figure, the latitude is restricted to near-equatorial values ($-10° < \text{lat} < +10°$) to eliminate the high-latitude points near noon that are well removed from the apex of the magnetosphere (this limitation removes ~14% of the data points, primarily from the region between 11 and 14 LT; see Figure 3b). In Figure 6a, the proton and electron temperatures are shown. Both clearly peak near local noon and decrease along the flanks, as the flow reaccelerates and adiabatically cools. It also appears that the prenoon temperatures, both proton and electron, tend to be somewhat higher than the postnoon temperatures. A similar dependence is seen in the $He^{++}$ temperature (not shown).

While it is possible that the prenoon/postnoon difference in the magnetosheath temperatures reveals different shock physics on the prenoon side of the bow shock versus the postnoon side, Figure 7 suggests that it is more likely the product of an accidental coupling between Cassini's orbital coverage and the solar wind speed. Figure 7 shows (in black) the solar wind speed predicted for Saturn's location by the University of Michigan mSWIM 1.5-D magnetohydrodynamic (MHD) model (Zieger & Hansen, 2008), with solar wind conditions observed at 1 AU as the boundary condition. The predicted speed is shown for the entire interval of this study, given in days from the start of 2004, as in Figure 2. Superimposed on the plot of the solar wind speed, with a vertical scale covering two decades rather than the one used for the solar wind, is the color-coded proton temperature from the magnetosheath data set. The color-coding is done according to the local time of the observation: light blue for $\text{LT} < 8$ or $\text{LT} > 16$, red for $8 < \text{LT} < 12$, and green for $12 < \text{LT} < 16$. At the bottom of the figure, the green zigzag curve shows $d\Phi$, the relative orbital phase between Saturn and Earth reported in the mSWIM files. Because mSWIM predicts the solar wind conditions at Saturn by using near-Earth observations as a boundary condition to the calculation, the prediction works best when Earth and Saturn are aligned radially (relative phase ~0°) (Zieger & Hansen, 2008).

Figure 7 shows rather clearly that throughout the time interval shown, and almost independent of $d\Phi$, the proton temperature tracks well the predicted solar wind speed. This is not unexpected since the role of the shock is to convert upstream bulk flow energy to downstream thermal energy, enabling magnetosonic waves to deflect the flow around the magnetospheric obstacle, so the higher the upstream flow energy, the higher the downstream temperature ought to be. The fact that the tracking works so well when one decade of speed variation is compared with two decades of temperature variation is consistent with the expectation that the magnetosheath temperature emerges from upstream flow energy (proportional to $V^2$). Comparison of the red (prenoon) and green (postnoon) points in Figure 7 reveals that the prenoon points were obtained primarily during times when the solar wind speed was high, whereas the postnoon points were obtained primarily during times when the solar wind speed was lower. Hence, the apparent local time dependence in Figure 6a is likely produced by the long-term variation in the solar wind speed. Although not shown here, the electron temperature and the $He^{++}$ temperature show a similarly good correspondence with the predicted solar wind speed.

Figure 6b shows the local time dependence of the proton-to-electron temperature ratio. While the prenoon values may be slightly higher than the postnoon values on average, the difference does not seem significant.

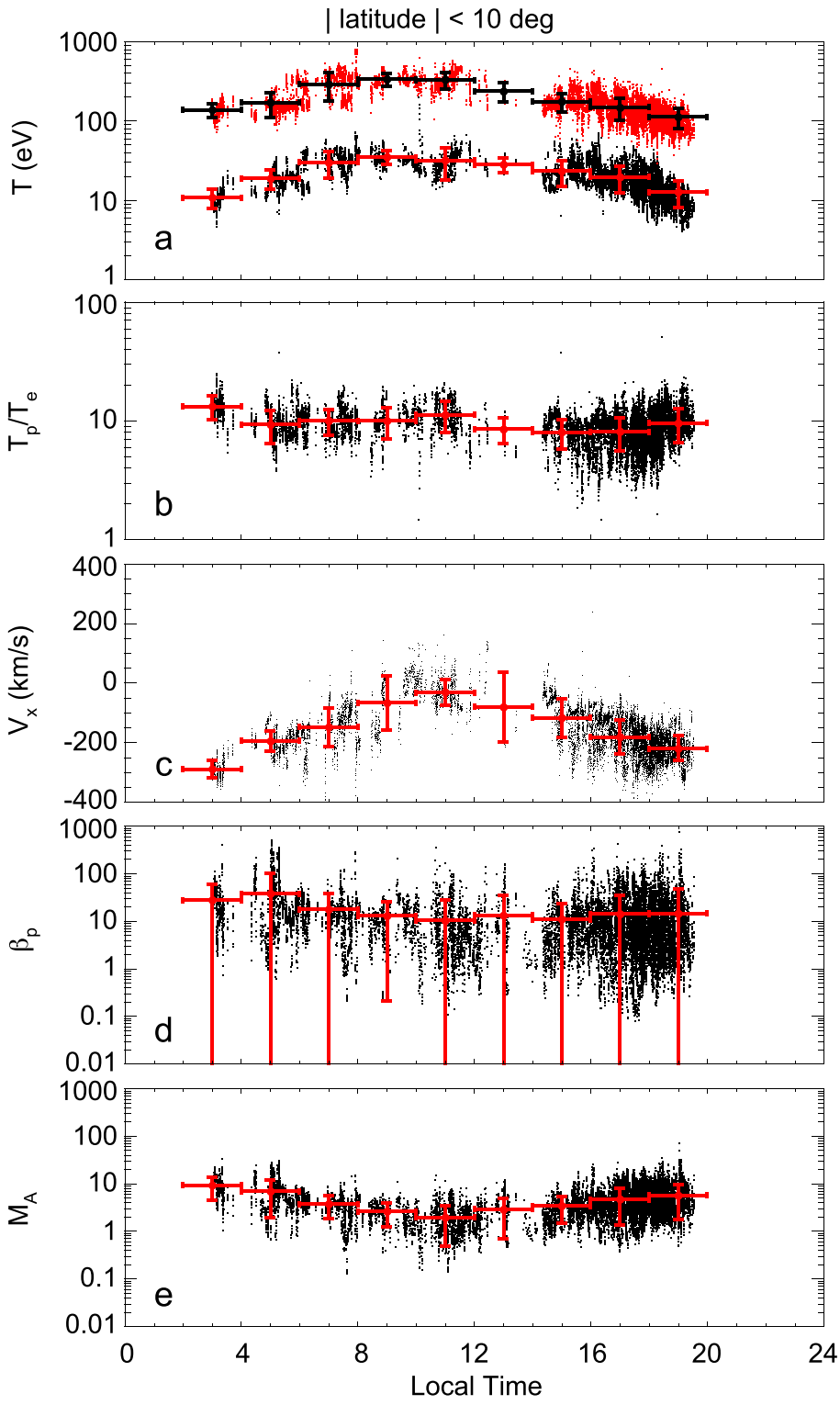


**Figure 6.** Local time dependence of various magnetosheath parameters at latitudes between −10° and +10°: (a) Proton (red) and electron (black) temperatures; (b) ratio of proton temperature to electron temperature; (c) SSQ *x* component of the measured flow velocity; (d) plasma proton beta; (e) Alfvén Mach number of the magnetosheath flow. Two-hour bin averages and standard deviations are also shown for all parameters.

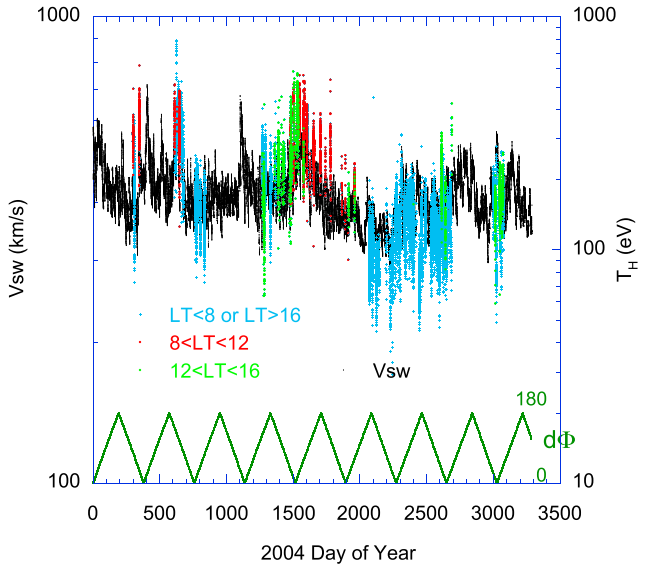


**Figure 7.** Solar wind speed predicted for Saturn's location by the mSWIM MHD model (black, left-hand scale), compared with the measured magnetosheath proton temperature (colored points, right-hand scale). Temperatures are color-coded according to local time of the measurement: light blue for LT $<$ 8 or LT $>$ 16, red for 8 $<$ LT $<$ 12, and green for 12 $<$ LT $<$ 16. Measurements in the 8–12 LT range appear to have been made primarily during times of elevated solar wind speed, whereas outside that range more measurements were made at lower values of the solar wind speed. The magnetosheath proton temperature tracks rather well the square of the predicted solar wind speed (two decades of $T_H$ variation for one decade of $V_{sw}$ variation). The green curve at the bottom of the plot shows the variation of the relative orbital phase between Saturn and Earth over the time interval. Intervals near d$\Phi \sim 0$ correspond to good radial alignment between Saturn and Earth and should provide the best model predictions at Saturn's orbit.

It is interesting that there is no decline in $T_p/T_e$ toward the flanks, where one would expect the bow shock to be weaker, and thus the electron share of the total temperature increase ($T_p + T_e$) to be larger (e.g., Schwartz et al., 1988, their Figure 6). This effect is probably seen only close to the bow shock itself; throughout the bulk of the magnetosheath, we are primarily seeing the adiabatic cooling of plasma that crossed the shock much closer to the nose.

Figure 6c shows the local time dependence of the XSSQ component of the measured flow velocity (negative is flow away from the Sun). Near the nose of the magnetosphere, the flow is strongly slowed or deflected, with a clear reacceleration along the flanks (see also Figure 5d). In these data it is not uncommon to find positive (sunward) values of $V_x$ near noon, presumably resulting from a rapid expansion of the magnetosphere in response to reduced solar wind dynamic pressure, as earlier reported for Jupiter (Richardson, 1987, 2002; Siscoe et al., 1980) but not heretofore for Saturn. Rapid expansions and contractions of the magnetopause are a consequence of the large compressibility of Saturn's magnetosphere (e.g., Achilleos et al., 2008; Arridge et al., 2006; Hansen et al., 2005).

Figure 6d shows that there is no strong dependence of proton $\beta$ on local time. Further, the variability in $\beta$ is very large, as indicated by the large error bars. This is largely because both the density and the field magnitude are highly variable, but their variations are not well correlated.

Figure 6e shows that the Alfvén Mach number is near and somewhat above 1 near the nose and increases along the flanks, largely mirroring the behavior of the flow velocity. The Alfvén speed itself (not shown) shows a tendency to decline toward the flanks, which further contributes to the rise in the Mach number there.

### 3.5. Estimation of Upstream Flow Speed

The clear correspondence between the magnetosheath proton temperature and the predicted solar wind speed seen in Figure 7 suggests that this temperature might provide a useful means of monitoring the upstream flow speed. Expanding the argument made above, the bulk flow energy brought into the bow shock by the upstream solar wind is converted at the shock to a combination of (slowed) flow energy, thermal energy, and magnetic field energy. Although the presence of the magnetospheric obstacle and its influence on the flow certainly affects the overall energy balance, one might nonetheless expect a rough equivalence between the upstream energy per particle and the downstream energy per particle. This possibility is explored in Figure 8. Figures 8a and 8d are color-coded plots of ($kT_p + 0.5m_pV^2$) and ($kT_p + 0.5m_pV^2 + B^2/8\pi n$), respectively, extracted from a global MHD simulation of Saturn's magnetosphere (Jia et al., 2012). The values of the combined energies per particle are normalized to the upstream bulk flow energy. The black dotted curve indicates the magnetopause identified in the simulation. In both cases (Figures 8a and 8d), the normalized summed energies appear rather constant throughout the magnetosheath, with values near 0.5. This is particularly true for the sum of the thermal and flow energies alone because the plasma beta is generally above 1 within the magnetosheath, so the contribution of the magnetic field energy to the overall sum is modest, except very near the magnetopause, where the field appears to build up in this simulation. An analysis of the total magnetosheath energy ($kT_p + 0.5m_pV^2 + B^2/8\pi n$) compared to the upstream bulk flow energy at several terrestrial bow shock crossings reported by Song et al. (1999) gives ratios ~0.4–0.6, quite similar to the Saturn simulation results in Figures 8a and 8d.

Figures 6a and 6c discussed above showed that both the proton temperature and the bulk flow speed in the magnetosheath vary with local time. However, their variations are opposite, and as shown in Figures 8b and 8e, the sum of the bulk flow energy and the proton thermal energy (with or without the magnetic energy) is

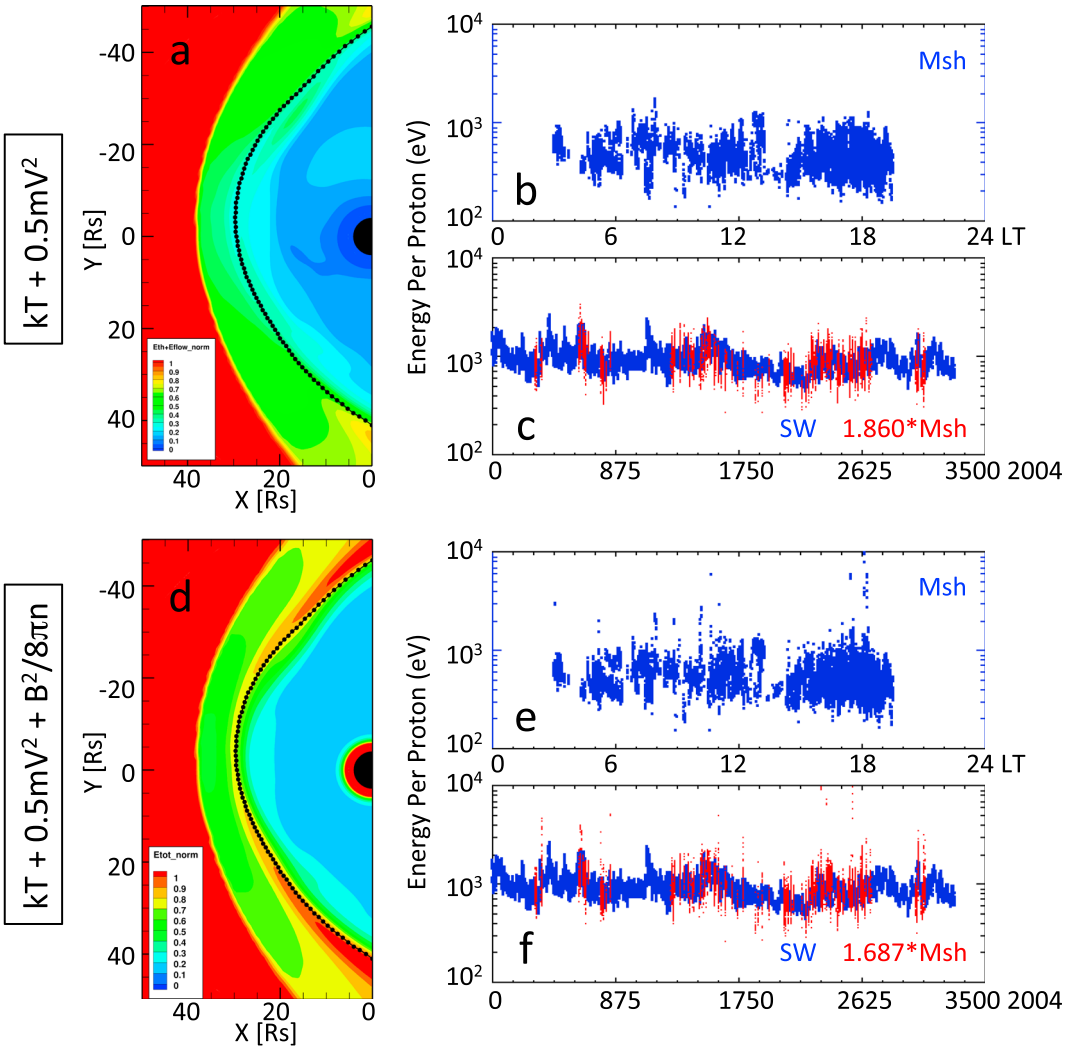


**Figure 8.** (a) Color-coded contours of ($kT_p + 0.5m_pV^2$) extracted from the global MHD simulation of Jia et al. (2012) and normalized to the upstream bulk flow energy. Throughout much of the dayside magnetosheath, the normalized energy sum lies between ~0.5 and 0.7. (b) Measured magnetosheath values of ($kT_p + 0.5m_pV^2$) versus local time for the new data set. (c) Solar wind bulk flow energy (blue) predicted for Saturn's location by the mSWIM MHD model, compared to 1.860 times the magnetosheath energy sum in panel (b) (red) as a function of day of year of 2004. (d–f) Same as (a–c), but for the total energy including the magnetic field ($kT_p + 0.5m_pV^2 + B^2/8\pi n$). For panel f, the magnetosheath energy is scaled by 1.687. In this calculation the energy per particle inside the magnetosphere (panels a and d) is significantly lower than it should be (by approximately the average mass of the ions) because all the ions in the single fluid are assumed to be protons.

essentially independent of local time. This suggests that the summed energy may be a suitable proxy for the solar wind speed. Averaging over our entire magnetosheath data set, we find that

$$< kT_p + 0.5m_pV^2 >= 478\pm153 \text{ eV}$$

and

$$< kT_p + 0.5m_pV^2 + B^2/8\,\pi n >= 527\pm182 \text{ eV}.$$

A similar average over the entire set of predicted solar wind speed from the mSWIM model (cf. Figure 7), interpolated to the magnetosheath measurement times, yields

$$< 0.5m_pV_{sw}{}^2 >= 889\pm253 \text{ eV}.$$

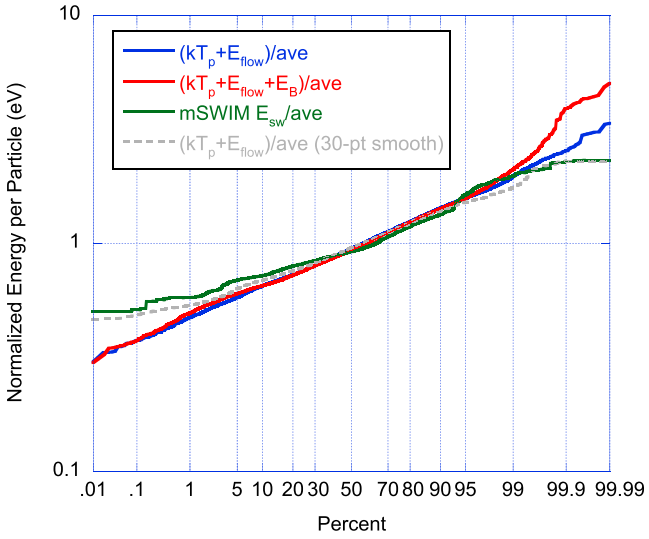


**Figure 9.** Probability distributions of magnetosheath thermal plus flow energy (blue) and total energy per particle (red) compared with that for the solar wind bulk flow energy per particle predicted by the mSWIM MHD model (green). The grey dashed curve is the distribution of the magnetosheath particle energy with a 30 pt smoothing applied. All quantities are normalized to their average over the entire CAPS data set.

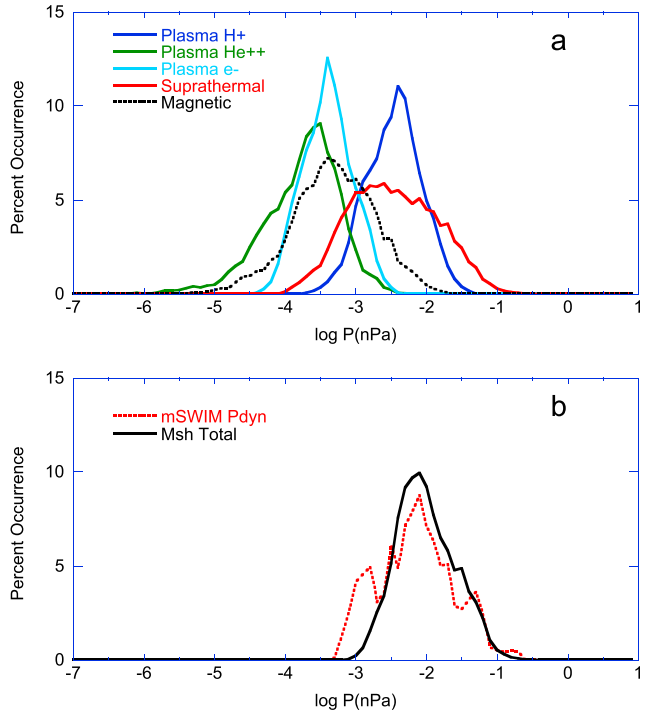


**Figure 10.** (a) Occurrence distribution of magnetosheath pressure contributions from various populations: Plasma protons (dark blue), plasma alpha particles (green), plasma electrons (light blue), suprathermal particles (red), and magnetic field (black dashed). (b) Occurrence distribution of summed components in panel (a) (black), compared with that for the bulk flow energy predicted by the mSWIM MHD model, interpolated to the magnetosheath data set points (red dashed).

Thus, on the average, the solar wind bulk flow energy is ~1.860 ± 0.797 times the combined magnetosheath bulk flow energy and proton temperature. Similarly, it is ~1.687 ± 0.755 times the combined magnetosheath bulk flow plus thermal plus magnetic energy per particle. In Figures 8c and 8f, 1.860 * ($kT_p$ + 0.5$m_pV^2$) and 1.687 * ($kT_p$ + 0.5$m_pV^2$ + $B^2/8\pi n$) are plotted in red over the solar wind bulk flow energy (0.5$m_pV_{sw}^2$) in blue. Both quantities show good tracking of the solar wind, with perhaps greater scatter when the magnetosheath magnetic field energy is included (as also reflected in the uncertainties in the ratios between the average values).

Confirming the statistical similarity of the magnetosheath energy per particle and the solar wind bulk flow energy per particle, Figure 9 shows the probability distribution of these parameters, normalized to their respective averages. For most of the range of normalized values, the shapes of the distributions are very similar. The magnetosheath distributions (red and blue curves) do deviate significantly from the solar wind distribution (green curve) at the high end and especially at the low end. However, this may be due to the higher time resolution of the magnetosheath measurements and their point-to-point variability. A 30 pt smoothing of the magnetosheath temperature plus flow energy (grey dashed curve) removes much of this deviation, and the distribution of smoothed values is extremely similar to the solar wind energy distribution.

Figures 8 and 9 thus suggest that we may estimate the upstream solar wind flow velocity from magnetosheath measurements with an average uncertainty of ~22% using the expressions 0.5$m_pV_{sw}^2$ = 1.860 * ($kT_p$ + 0.5$m_pV^2$) or 0.5$m_pV_{sw}^2$ = 1.687 * ($kT_p$ + 0.5$m_pV^2$ + $B^2/8\pi$n). At this point, both expressions yield roughly equally good matches to the upstream velocity distribution (Figure 9), with no clear preference between them. In section 4, we explore the utility of the first expression as our proxy.

### 3.6. Pressure Contributions

In their study of Saturn's magnetosheath properties, Sergis et al. (2013) found that the energetic particles in the MIMI energy range frequently contribute half or more of the total magnetosheath thermal pressure. Figure 10a shows the statistical distribution of magnetosheath thermal pressure contributed by various populations and by the magnetic field in the new data set. It is very similar to Figure 8 of Sergis et al. (2013). Figure 10b compares the distribution of the total thermal/magnetic magnetosheath pressure (thermal protons + alphas + electrons + suprathermal + magnetic) to the distribution of solar wind dynamic pressures predicted by the mSWIM model, interpolated to the magnetosheath measurement points. Figure 10b confirms that on average, with the observed energy partition, pressure balance exists between the magnetosheath and the incident solar wind.

## 4. Sample Applications

### 4.1. Magnetosheath Structure

The magnetic structure of the magnetosheath has been thoroughly examined by Sulaiman et al. (2014, 2017) using Cassini MAG data from 2004 to 2010. They found evidence of significant polar flattening of the magnetopause. They also found that the *z* component of the

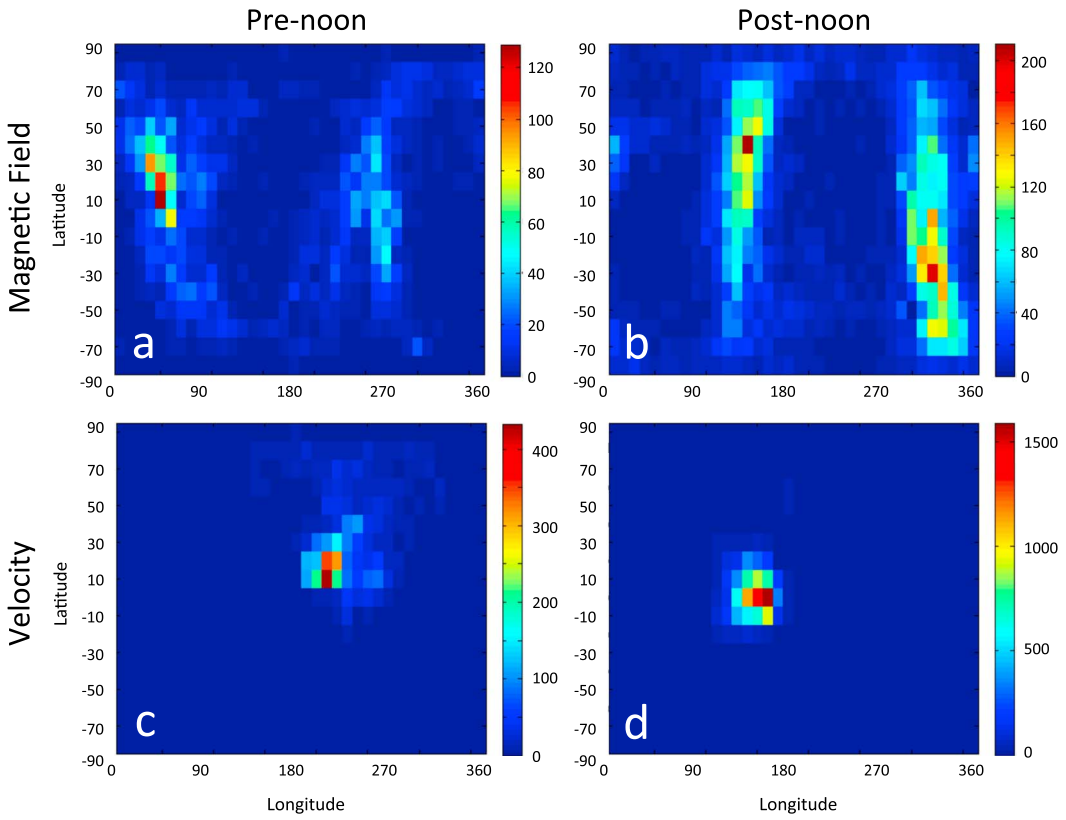


**Figure 11.** (a) Binned occurrence of magnetic field latitude and longitude for prenoon magnetosheath observations. (b) Same for postnoon observations. (c) Similar plot of velocity latitude and longitude for prenoon observations. (d) Same for postnoon. Longitude and latitude are defined in the SSQ coordinate system. Longitudes ~180° correspond to antisunward flow, dawnward flow has longitudes ~270°, and duskward flow would have longitudes ~90°. Prenoon flows are deflected dawnward, and postnoon flows are deflected duskward, as expected.

magnetosheath magnetic field (which they termed the "meridional component") was frequently larger than would be expected from simple draping of the largely Parker-spiral magnetic field of the upstream solar wind (Jackman & Arridge, 2011; Jackman, Forsyth, & Dougherty, 2008). They attribute this to a combination of the nonaxisymmetry of the flattened magnetopause (Erkaev et al., 1996; Farrugia et al., 1998) and a field-flow coupling in which the plasma flow over the obstacle twists the magnetic field, as inferred from terrestrial magnetosheath observations (Longmore et al., 2006). As explained by Erkaev et al. and Farrugia et al., polar flattening of the magnetopause produces stronger pressure gradients out of the equatorial plane than in the plane, leading to greater acceleration of the flow out of the plane and more pronounced field stretching in that direction.

Figures 11a and 11b, using data from our new magnetosheath data set, largely reproduce the results shown in Figure 2 of Sulaiman et al. (2014). These figures show the magnetic field longitude (their "azimuthal angle") and latitude (their "meridional angle") for the prenoon and postnoon measurements in our data set. There are slight differences from the results of Sulaiman et al. due to the use of a different coordinate system and to our inclusion of data from 2011 and 2012, largely from the dusk flank. As shown by Sulaiman et al., the preferred longitudes of the field are consistent with draping of a largely equatorial interplanetary magnetic field, but there is a significant extension of the latitude occurrence to nonequatorial orientations.

Figures 11c and 11d show the corresponding observed velocity vector orientations for the prenoon and postnoon sectors. Respectively, they clearly show the dawnward and duskward deflections expected for flow around the magnetospheric obstacle (see also Figure 5). There is a weak halo of more strongly deflected flows in the prenoon panel (Figure 11c) that is attributable to the few high-latitude measurements

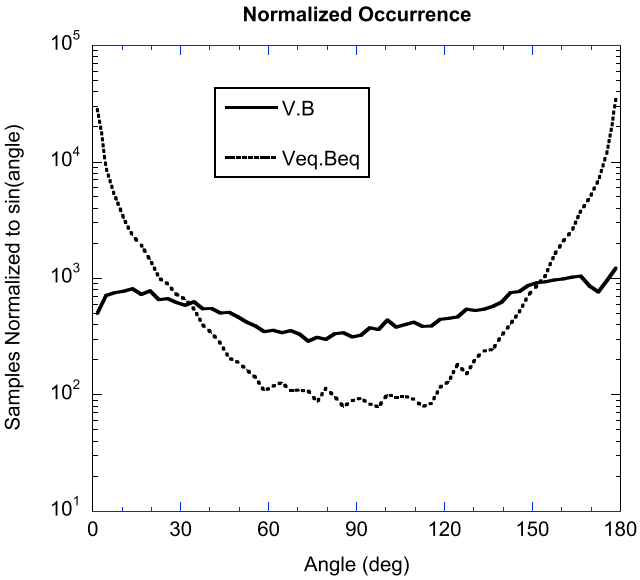


**Figure 12.** Occurrence distribution of the angle between the full magnetic field vector and the full velocity vector (solid curve) compared with that for the equatorial projections of both vectors (dashed curve). Both distributions have been divided by the sine of the angle, which is proportional to the distribution for a random orientation between the vectors. The equatorial components are rather strongly aligned, but inclusion of the *z* components of both vectors significantly reduces the total vector alignment.

in the data set (e.g., Figure 5b), but otherwise the observed flow direction is better confined to the equatorial plane than is the magnetic field.

Figure 12 shows the occurrence distribution of the angle between the flow and the magnetic field. The solid curve shows the distribution of the angle between the total field and flow velocities, while the dashed curve shows the distribution of the angle between just the equatorial components of both vectors. Both distributions have been normalized by the sine of the angle, which is proportional to the likelihood that a randomly oriented pair of vectors will have a particular angle between them. As shown by the dashed curve, there is a strong tendency for the equatorial components of the field and flow to be aligned (peaks near angles of 0° and 180°). However, when the *z* components of both vectors are included, the field and flow are found to be only weakly aligned (solid curve). Thus, it appears that the tendency for the field to be pulled out of the equatorial orientation by flows at higher latitudes as noted by Sulaiman et al. (2014, 2017) may appreciably affect the field-flow alignment in the equatorial region, which would tend to enhance the growth of the K-H instability there (Desroche et al., 2013).

### 4.2. Shock Heating

As mentioned in the introduction, the partition of bulk flow energy into downstream particle thermal energy at a collisionless shock is one of the fundamental issues for shock physics. Indications from terrestrial bow shock studies indicate that the fraction that goes into electron heating declines with upstream Mach number (e.g., Schwartz et al., 1988), so the higher-than-terrestrial Mach numbers of Saturn's bow shock offer the opportunity to explore the electron heating in a parameter regime not frequently accessible at the Earth. In a careful study of 94 bow shock crossings at Saturn, Masters et al. (2011) showed that between ~3 and ~7% (median of 4.3%) of the incident bulk flow energy normal to the shock is converted to electron heating and that this fraction decreases with increasing upstream $M_A$. Lacking an upstream solar wind monitor, they used the mSWIM model predictions of the solar wind flow speed, and they estimated the upstream density based on the observed magnetosheath density and an assumed compression ratio of 4 ± 1 across the shock. They also tried to take into account the motion of the shock itself, which makes a significant difference in the upstream flow speed.

The large set of magnetosheath electron temperature measurements in our data set, combined with the statistically based estimates of the upstream flow speed discussed above, allows us to explore how the magnetosheath temperature relates to the solar wind bulk flow energy, at least in a statistical sense. In general, our measurements are not made close to a shock crossing, so we have no information about the shock motion. On the average, however, the shock moves out as much as it moves in, so if we simply neglect the shock motion, that neglect should only introduce an uncertainty in the estimated upstream flow speed. Indeed, this spread is essentially already included in our estimated speed since the scaling of magnetosheath total energy to upstream flow energy on which it is based similarly ignores the shock speed.

Figure 6a showed that the magnetosheath electron temperature depends fairly strongly on local time, but we argued above that this variation is probably predominantly due to adiabatic cooling of plasma that crossed the shock not far from the nose. Thus, we can use the average local time dependence of the full data set to scale each observed measurement to what it would have been immediately after transiting the shock near the nose. Accordingly, we find that the local time dependence of $T_e$ shown in Figure 6a can be well represented as

$$T_{e,fit} = 18.826 + 15.068\cos(\mathrm{LT} - 11.053) \quad (3)$$

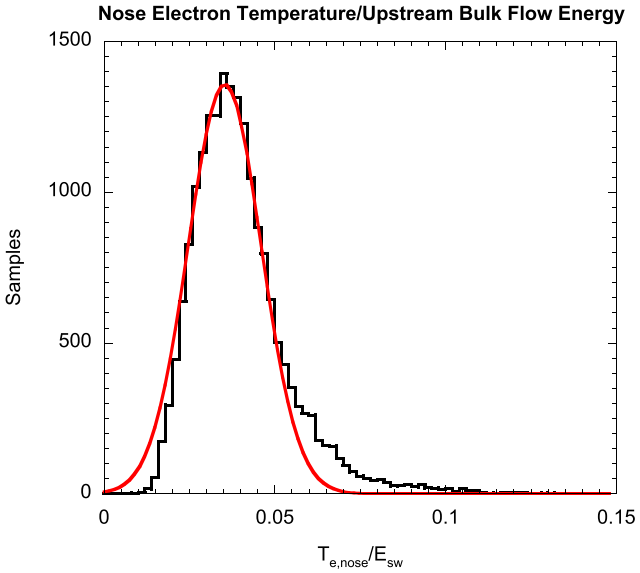


**Figure 13.** Occurrence distribution of magnetosheath electron temperature (black) scaled to the nose of the magnetosphere (equation (4)) and normalized to the upstream bulk flow energy estimated from the total magnetosheath kinetic energy (equation (5)). The red curve is a Gaussian fit to the distribution, with a peak at 3.5 ± 1.5%.

From each measurement point ($T_e$, LT), we can then estimate the corresponding temperature near the nose of the shock (actually, near 11.053 LT, which is where the average temperature reaches a maximum in LT) as

$$T_{e,nose} = \left[T_e(\mathrm{LT})/T_{e,fit}(\mathrm{LT})\right] \cdot T_{e,fit}(11.053\ \mathrm{LT}) \quad (4)$$

Scaled in this way, the nose electron temperature is correlated with the estimated upstream bulk flow energy with a correlation coefficient of ~0.44. Figure 13 shows the occurrence distribution of $T_{e,nose}/E_{sw}$, where we have used

$$E_{sw} = 0.5 m_p V_{sw}^2 = 1.860^* \left(kT_p + 0.5 m_p V^2\right) \quad (5)$$

as discussed above. A Gaussian fit to this distribution (red curve) yields a peak at 3.5 ± 1.5% with $R = 0.99$. The median of 3.8% is consistent with the findings of Masters et al. (2011), but we find a smaller spread in the values than that study. These values of $T_{e,nose}/E_{sw}$ are smaller than the typical value of ~7% at the terrestrial bow shock (Schwartz et al., 1988; Thomsen et al., 1987).

Strictly speaking, the ratio we should be calculating is the change in electron temperature across the shock, compared to the drop in bulk flow energy normal to the shock (e.g., Schwartz et al., 1988). However, at Saturn the upstream electron temperature is extremely low, typically below the ability of ELS to measure it in the presence of the spacecraft photoelectrons below ~3 eV. Hence, to within a few percent, the change in electron temperature can be well approximated by the downstream temperature alone. Similarly, for crossings near the nose, the downstream bulk flow energy is typically only ~10% of the upstream value, so approximating the drop in flow energy by the upstream energy alone probably only results in an ~10% underestimate of the heating ratio. Accounting for these factors, the typical fraction of electron heating is probably closer to 4 than 3.5, still significantly lower than the typical value for the generally lower-Mach-number shocks at the Earth.

## 5. Summary

We have introduced a new Cassini magnetosheath data set that is based on a comprehensive survey of intervals in which the observed magnetosheath flow was encompassed within the CAPS FOV and for which the numerical moments are therefore expected to be accurate. In addition, we have merged this data set with corresponding time averages of the electron moments (density and temperature) from the CAPS Electron Spectrometer, energetic particle pressures from MIMI, and magnetic field measurements from the Cassini MAG. The data set includes 657 separate magnetosheath intervals, comprising a total of 19,155 valid measurements (2,213 hr). For a relatively small number of these intervals, one or more of the other Cassini instruments may not have returned valid data, and in the accompanying supporting information, these data entries are marked with fill values.

We have used this data set to explore the statistical behavior of a number of relevant magnetosheath properties, both to validate the data by comparison with previous results and to demonstrate the range of useful applications. With a much expanded set of data compared to what was previously available, we have been able to examine the local time dependence of various magnetosheath properties and to show that some of what appears to be a local time dependence may in fact be an artifact of the coupling between the local time coverage and variations in the upstream solar wind velocity, which is of primary importance in determining the magnetosheath properties.

Using the statistical similarity of the total downstream energy per particle (thermal + flow + magnetic) and the upstream bulk flow energy per particle, as predicted by the University of Michigan mSWIM MHD model (Zieger & Hansen, 2008), we have proposed a new means of approximating the upstream flow speed corresponding to any given magnetosheath measurement. This procedure helps mitigate the absence of an upstream solar wind monitor.

Using the estimated upstream flow energy, and assuming that most of the magnetosheath plasma we observe actually crossed the bow shock fairly near to the nose, we find that the electron heating at Saturn's bow shock represents ~4% of the bulk flow energy lost across the shock, less than the typical terrestrial value of ~7%, and consistent with expectations of the Mach-number dependence of electron heating.

We have also shown that there is a strong tendency for the equatorial components of the magnetosheath magnetic field and flow to be aligned, but when the *z* components of both vectors are included, the field and flow are found to be only weakly aligned. Thus, we confirm the tendency for the field to be pulled out of the equatorial orientation by flows at higher latitudes, as noted previously (e.g., Sulaiman et al., 2014, 2017). Such an effect reduces the field-flow alignment in the equatorial region, perhaps enhancing the growth of the K-H instability.

## 6. Conclusions

Results presented here offer a more comprehensive picture of the nature of Saturn's magnetosheath and its relation to the properties of the upstream solar wind than has been possible in the past. It is hoped that this new data set, available as supporting information to this paper, will enable new insights into the interaction of the solar wind and Saturn's magnetosphere.

**Acknowledgments**

This work emerged from collaborative discussions that took place during a visit of MFT to the University of Southampton as a Diamond Jubilee Fellow. The support provided by the Diamond Jubilee Fellowship is gratefully acknowledged. Work at PSI was supported by the NASA Cassini program through JPL contract 1243218 with Southwest Research Institute. The Cassini project is managed by the Jet Propulsion Laboratory for NASA. C. M. J. is supported by Science and Technology Facilities Council Ernest Rutherford Fellowship number ST/L004399/1. A. J. C. acknowledges support from the STFC consolidated grants to UCL-MSSL ST/K000977/1 and ST/N000722/1, and thanks ESA and the UK Space Agency for support of CAPS-ELS operations until 2012. Work at the Academy of Athens was supported by contract no 144247 between JHU/APL and the Academy of Athens. Work by X. J. is supported by NASA through grant NNX15AH28G. All Cassini magnetometer, energetic particle, and plasma data used for this study are available from the Planetary Data System (http://pds.nasa.gov/) and are included in the electronic supplement to this paper. The mSWIM predictions of solar wind properties are publicly available on the University of Michigan Web site (http://mswim.engin.umich.edu/).

## References

Achilleos, N., Arridge, C. S., Bertucci, C., Jackman, C. M., Dougherty, M. K., Khurana, K. K., & Russell, C. T. (2008). Large-scale dynamics of Saturn's magnetopause: Observations by Cassini. *Journal of Geophysical Research*, *113*, A11209. https://doi.org/10.1029/2008JA013265

Arridge, C. S., Achilleos, N., Dougherty, M. K., Khurana, K. K., & Russell, C. T. (2006). Modeling the size and shape of Saturn's magnetopause with variable dynamic pressure. *Journal of Geophysical Research*, *111*, A11227. https://doi.org/10.1029/2005JA011574

Burkholder, B., Delamere, P. A., Ma, X., Thomsen, M. F., Wilson, R. J., & Bagenal, F. (2017). Local time asymmetry of Saturn's magnetosheath flows. *Geophysical Research Letters*, *44*, 5877–5883. https://doi.org/10.1002/2017GL073031

Delamere, P. A., Wilson, R. J., Eriksson, S., & Bagenal, F. (2013). Magnetic signatures of Kelvin-Helmholtz vortices on Saturn's magnetopause: Global survey. *Journal of Geophysical Research: Space Physics*, *118*, 393–404. https://doi.org/10.1029/2012JA018197

Delamere, P. A., Wilson, R. J., & Masters, A. (2011). Kelvin-Helmholtz instability at Saturn's magnetopause: Hybrid simulations. *Journal of Geophysical Research*, *116*, A10222. https://doi.org/10.1029/2011JA016724

Desroche, M., Bagenal, F., Delamere, P. A., & Erkaev, N. (2013). Conditions at the magnetopause of Saturn and implications for the solar wind interaction. *Journal of Geophysical Research: Space Physics*, *118*, 3087–3095. https://doi.org/10.1002/jgra.50294

Dougherty, M. K., Kellock, S., Southwood, D. J., Balogh, A., Smith, E. J., Tsurutani, B. T., et al. (2004). The Cassini magnetic field investigation. *Space Science Reviews*, *114*(1-4), 331–383. https://doi.org/10.1007/s11214-004-1432-2

Erkaev, N. V., Farrugia, C. J., & Biernat, H. K. (1996). Effects on the Jovian magnetosheath arising from solar wind flow around nonaxisymmetric bodies. *Journal of Geophysical Research*, *101*, 10,665–10,672. https://doi.org/10.1029/95JA03518

Farrugia, C. J., Biernat, H. K., & Erkaev, N. V. (1998). The effect of the magnetopause shapes of Jupiter and Saturn on magnetosheath parameters. *Planetary and Space Science*, *46*(5), 507–514. https://doi.org/10.1016/S0032-0633(97)00225-0

Fuselier, S. A., Frahm, R., Lewis, W. S., Masters, A., Mukherjee, J., Petrinec, S. M., & Sillanpaa, I. J. (2014). The location of magnetic reconnection at Saturn's magnetopause: A comparison with Earth. *Journal of Geophysical Research: Space Physics*, *119*, 2563–2578. https://doi.org/10.1002/2013JA019684

Gurnett, D. A., Kurth, W. S., Kirchner, D. L., Hospodarsky, G. B., Averkamp, T. F., Zarka, P., et al. (2004). The Cassini Radio and Plasma Wave Science Investigation. *Space Science Reviews*, *114*(1-4), 395–463. https://doi.org/10.1007/s11214-004-1434-0

Hadid, L. Z., Sahraoui, F., Kiyani, K. H., Retinò, A., Modolo, R., Canu, P., et al. (2015). Nature of the MHD and kinetic scale turbulence in the magnetosheath of Saturn. *Astrophysical Journal Letters*, *813*(2), L29. https://doi.org/10.1088/2041-8205/813/2/L29

Hansen, K. C., Ridley, A. J., Hospodarsky, G. B., Achilleos, N., Dougherty, M. K., Gombosi, T. I., & Tóth, G. (2005). Global MHD simulations of Saturn's magnetosphere at the time of Cassini approach. *Geophysical Research Letters*, *32*, L20S06. https://doi.org/10.1029/2005GL022835

Jackman, C. M., & Arridge, C. S. (2011). Solar cycle effects on the dynamics of Jupiter's and Saturn's magnetospheres. *Solar Physics*, *274*(1-2), 481–502. https://doi.org/10.1007/s11207-011-9748-z

Jackman, C. M., Forsyth, R. J., & Dougherty, M. K. (2008). The overall configuration of the interplanetary magnetic field upstream of Saturn as revealed by Cassini observations. *Journal of Geophysical Research*, *113*, A08114. https://doi.org/10.1029/2008JA013083

Jia, X., Hansen, K. C., Gombosi, T. I., Kivelson, M. G., Tóth, G., DeZeeuw, D. L., & Ridley, A. J. (2012). Magnetospheric configuration and dynamics of Saturn's magnetosphere: A global MHD simulation. *Journal of Geophysical Research*, *117*, A05225. https://doi.org/10.1029/2012JA017575

Kanani, S. J., Arridge, C. S., Jones, G. H., Fazakerley, A. N., McAndrews, H. J., Sergis, N., et al. (2010). A new form of Saturn's magnetopause using a dynamic pressure balance model, based on in situ, multi-instrument Cassini measurements. *Journal of Geophysical Research*, *115*, A06207. https://doi.org/10.1029/2009JA014262

Kivelson, M. G., & Jia, X. (2014). Control of periodic variations in Saturn's agnetosphere by compressional waves. *Journal of Geophysical Research: Space Physics*, *119*, 8030–8045. https://doi.org/10.1002/2014JA020258

Krimigis, S. M., Mitchell, D. G., Hamilton, D. C., Livi, S., Dandouras, J., Jaskulek, S., et al. (2004). Magnetosphere Imaging Instrument (MIMI) on the Cassini Mission to Saturn/Titan. *Space Science Reviews*, *114*(1-4), 233–329. https://doi.org/10.1007/s11214-004-1410-8

Lavraud, B., Borovsky, J. E., Génot, V., Schwartz, S. J., Birn, J., Fazakerley, A. N., et al. (2009). Tracing solar wind plasma entry into the magnetosphere using ion-to-electron temperature ratio. *Geophysical Research Letters*, *36*, L18109. https://doi.org/10.1029/2009GL039442

Lewis, G. R., André, N., Arridge, C. S., Coates, A. J., Gilbert, L. K., Linder, D. R., & Rymer, A. M. (2008). Derivation of density and temperature from the Cassini-Huygens CAPS electron spectrometer. *Planetary and Space Science*, *56*(7), 901–912. https://doi.org/10.1016/j.pss.2007.12.017

Linder, D. R., Coates, A. J., Woodliffe, R. D., Alsop, C., Johnstone, A. D., Grande, et al. (1998). In F. Pfaff, J. E. Borovsky, & D. T. Young (Eds.), *Measurement Techniques in Space Plasmas: Particles, Geophysics Monograph Series* (Vol. 102, pp. 257–262). American Geophysical Union.

Longmore, M., Schwartz, S. J., & Lucek, E. A. (2006). Rotation of the magnetic field in Earth's magnetosheath by bulk magnetosheath plasma flow. *Annales Geophysicae*, *24*(1), 339–354. https://doi.org/10.5194/angeo-24-339-2006

Ma, X., Stauffer, B., Delamere, P. A., & Otto, A. (2015). Asymmetric Kelvin-Helmholtz propagation at Saturn's dayside magnetopause. *Journal of Geophysical Research*, *120*, 1867–1875. https://doi.org/10.1002/2014JA020746

Masters, A., Achilleos, N., Bertucci, C., Dougherty, M. K., Kanani, S. J., Arridge, C. S., et al. (2009). Surface waves on Saturn's dawn flank magnetopause driven by the Kelvin-Helmholtz instability. *Planetary and Space Science*, *57*(14-15), 1769–1778. https://doi.org/10.1016/j.pss.2009.02.010

Masters, A., Achilleos, N., Cutler, J. C., Coates, A. J., Dougherty, M. K., & Jones, G. H. (2012). Surface waves on Saturn's magnetopause. *Planetary and Space Science*, *65*(1), 109–121. https://doi.org/10.1016/j.pss.2012.02.007

Masters, A., Achilleos, N., Dougherty, M. K., Slavin, J. A., Hospodarsky, G. B., Arridge, C. S., & Coates, A. J. (2008). An empirical model of Saturn's bow shock: Cassini observations of shock location and shape. *Journal of Geophysical Research*, *113*, A10210. https://doi.org/10.1029/2008JA013276

Masters, A., Achilleos, N., Kivelson, M. G., Sergis, N., Dougherty, M. K., Thomsen, M. F., et al. (2010). Cassini observations of a Kelvin-Helmholtz vortex in Saturn's outer magnetosphere. *Journal of Geophysical Research*, *115*, A07225. https://doi.org/10.1029/2010JA015351

Masters, A., Eastwood, J. P., Swisdak, M., Thomsen, M. F., Russell, C. T., Sergis, N., et al. (2012). The importance of plasma β conditions for magnetic reconnection at Saturn's magnetopause. *Geophysical Research Letters*, *39*, L08103. https://doi.org/10.1029/2012GL051372

Masters, A., Phan, T. D., Badman, S. V., Hasegawa, H., Fujimoto, M., Russell, C. T., et al. (2014). The plasma depletion layer in Saturn's magnetosheath. *Journal of Geophysical Research: Space Physics*, *119*, 121–130. https://doi.org/10.1002/2013JA019516

Masters, A., Schwartz, S. J., Henley, E. M., Thomsen, M. F., Zieger, B., Coates, A. J., et al. (2011). Electron heating at Saturn's bow shock. *Journal of Geophysical Research*, *116*, A10107. https://doi.org/10.1029/2011JA016941

Masters, A., Sulaiman, A. H., Sergis, N., Stawarz, L., Fujimoto, M., Coates, A. J., & Dougherty, M. K. (2016). Suprathermal electrons at Saturn's bow shock. *Astrophysical Journal*, *826*(1), 48. https://doi.org/10.3847/0004-637X/826/1/48

Phan, T.-D., Paschmann, G., Baumjohann, W., & Sckopke, N. (1994). The magnetosheath region adjacent to the dayside magnetopause: AMPTE/IRM observations. *Journal of Geophysical Research*, *99*, 121–141. https://doi.org/10.1029/93JA02444

Pilkington, N. M., Achilleos, N., Arridge, C. S., Guio, P., Masters, A., Ray, L. C., et al. (2015). Asymmetries observed in Saturn's magnetopause geometry. *Geophysical Research Letters*, *42*, 6890–6898. https://doi.org/10.1002/2015GL065477

Pilkington, N. M., Achilleos, N., Arridge, C. S., Masters, A., Sergis, N., Coates, A. J., & Dougherty, M. K. (2014). Polar confinement of Saturn's magnetosphere revealed by in situ Cassini observations,. *Journal of Geophysical Research: Space Physics*, *119*, 2858–2875. https://doi.org/10.1002/2014JA019774

Richardson, J. D. (1987). Ion distribution functions in the dayside magnetosheaths of Jupiter and Saturn. *Journal of Geophysical Research*, *92*, 6133–6140. https://doi.org/10.1029/JA092iA06p06133

Richardson, J. D. (2002). The magnetosheaths of the outer planets. *Planetary and Space Science*, *50*(5-6), 503–517. https://doi.org/10.1016/S0032-0633(02)00029-6

Schwartz, S. J., Thomsen, M. F., Bame, S. J., & Stansberry, J. (1988). Electron heating and the potential jump across fast mode shocks. *Journal of Geophysical Research*, *93*, 12,923–12,931. https://doi.org/10.1029/JA093iA11p12923

Sergis, N., Jackman, C. M., Masters, A., Krimigis, S. M., Thomsen, M. F., Hamilton, D. C., et al. (2013). Particle and magnetic field properties of the Saturnian magnetosheath: Presence and upstream escape of hot magnetospheric plasma. *Journal of Geophysical Research*, *118*, 1620–1634. https://doi.org/10.1002/jgra.50164

Sergis, N., Jackman, C. M., Thomsen, M. F., Krimigis, S. M., Mitchell, D. G., Hamilton, D. C., et al. (2017). Radial and local time structure of the Saturnian ring current, revealed by Cassini. *Journal of Geophysical Research: Space Physics*, *122*, 1803–1815. https://doi.org/10.1002/2016JA023742

Sergis, N., Krimigis, S. M., Mitchell, D. G., Hamilton, D. C., Krupp, N., Mauk, B. H., et al. (2009). Energetic particle pressure in Saturn's magnetosphere measured with the Magnetospheric Imaging Instrument on Cassini. *Journal of Geophysical Research*, *114*, A02214. https://doi.org/10.1029/2008JA013774

Siscoe, G. L., Crooker, N. U., & Belcher, J. W. (1980). Sunward flow in Jupiter's magnetosheath. *Geophysical Research Letters*, *7*, 25–28. https://doi.org/10.1029/GL007i001p00025

Slavin, J. A., Smith, E. J., Spreiter, J. R., & Stahara, S. S. (1985). Solar wind flow about the outer planets: Gas dynamic modeling of the Jupiter and Saturn bow shocks. *Journal of Geophysical Research*, *90*, 6275–6286. https://doi.org/10.1029/JA090iA07p06275

Song, P., Russell, C. T., Zhang, X. X., Stahara, S. S., Spreiter, J. R., & Gombosi, T. I. (1999). On the processes in the terrestrial magnetosheath 2. Case study. *Journal of Geophysical Research*, *104*, 22,357–22,373. https://doi.org/10.1029/1999JA900246

Stahara, S. S., Spreiter, J. R., Rachiele, R., & Slavin, J. A. (1989). A three-dimensional gasdynamic model for solar wind flow past nonaxisymmetric magnetospheres: Application to Jupiter and Saturn. *Journal of Geophysical Research*, *94*, 13,353–13,365. https://doi.org/10.1029/JA094iA10p13353

Sulaiman, A. H., Jia, X., Achilleos, N., Sergis, N., Gurnett, D. A., & Kurth, W. S. (2017). Large-scale solar wind flow around Saturn's nonaxisymmetric magnetosphere. *Journal of Geophysical Research: Space Physics*, *122*, 9198–9206. https://doi.org/10.1002/2017JA024595

Sulaiman, A. H., Masters, A., & Dougherty, M. K. (2016). Characterization of Saturn's bow shock: Magnetic field observations of quasi-perpendicular shocks. *Journal of Geophysical Research*, *121*, 4425–4434. https://doi.org/10.1002/2016JA022449

Sulaiman, A. H., Masters, A., Dougherty, M. K., Burgess, D., Fujimoto, M., & Hospodarsky, G. B. (2015). Quasiperpendicular high Mach number shocks. *Physical Review Letters*, *115*(12), 125001. https://doi.org/10.1103/PhysRevLett.115.125001

Sulaiman, A. H., Masters, A., Dougherty, M. K., & Jia, X. (2014). The magnetic structure of Saturn's magnetosheath. *Journal of Geophysical Research*, *119*, 5651–5661. https://doi.org/10.1002/2014JA020019

Thomsen, M. F., Mellott, M. M., Stansberry, J. A., Bame, S. J., Gosling, J. T., & Russell, C. T. (1987). Strong electron heating at the Earth's bow shock. *Journal of Geophysical Research*, *92*, 10,119–10,124. https://doi.org/10.1029/JA092iA09p10119

Thomsen, M. F., Reisenfeld, D. B., Delapp, D. M., Tokar, R. L., Young, D. T., Crary, F. J., et al. (2010). Survey of ion plasma parameters in Saturn's magnetosphere. *Journal of Geophysical Research*, *115*, A10220. https://doi.org/10.1029/2010JA015267

Went, D. R., Hospodarsky, G. B., Masters, A., Hansen, K. C., & Dougherty, M. K. (2011). A new semiempirical model of Saturn's bow shock based on propagated solar wind parameters. *Journal of Geophysical Research*, *116*, A07202. https://doi.org/10.1029/2010JA016349

Young, D. T., Berthelier, J. J., Blanc, M., Burch, J. L., Coates, A. J., Goldstein, R., et al. (2004). Cassini plasma spectrometer investigation. *Space Science Reviews*, *114*(1-4), 1–112. https://doi.org/10.1007/s11214-004-1406-4

Zieger, B., & Hansen, K. C. (2008). Statistical validation of a solar wind propagation model from 1 to 10 AU. *Journal of Geophysical Research*, *113*, A08107. https://doi.org/10.1029/2008JA013046